Idealized Study of Ocean Impacts on Tropical Cyclone Intensity Forecasts

G. R. HALLIWELL JR.

Physical Oceanography Division, NOAA/Atlantic Oceanographic and Meteorological Laboratory, Miami, Florida

S. GOPALAKRISHNAN AND F. MARKS

Hurricane Research Division, NOAA/Atlantic Oceanographic and Meteorological Laboratory, Miami, Florida

D. WILLEY

Cooperative Institute for Marine and Atmospheric Studies, University of Miami, Miami, Florida

ABSTRACT

Idealized coupled tropical cyclone (TC) simulations are conducted to isolate ocean impacts on intensity forecasts. A one-dimensional ocean model is embedded into the Hurricane Weather Research and Forecasting (HWRF) mesoscale atmospheric forecast model. By inserting an initial vortex into a horizontally uniform atmosphere above a horizontally uniform ocean, the SST cooling rate becomes the dominant large-scale process controlling intensity evolution. Westward storm translation is introduced by bodily advecting ocean fields toward the east. The ocean model produces a realistic cold wake structure allowing the sensitivity of quasi-equilibrium intensity to storm (translation speed, size) and ocean (heat potential) parameters to be quantified. The atmosphere provides feedback through adjustments in 10-m temperature and humidity that reduce SST cooling impact on quasi-equilibrium intensity by up to 40%. When storms encounter an oceanic region with different heat potential, enthalpy flux adjustment is governed primarily by changes in air–sea temperature and humidity differences that respond within 2–4 h in the inner-core region, and secondarily by wind speed changes occurring over a time interval up to 18 h after the transition. Atmospheric feedback always acts to limit the change in enthalpy flux and intensity through adjustments in 10-m temperature and humidity. Intensity change is asymmetric, with a substantially smaller increase for storms encountering larger heat potential compared to the decrease for storms encountering smaller potential. The smaller increase results initially from the smaller wind speed present at the transition time plus stronger limiting atmospheric feedback. The smaller wind speed increase resulting from these two factors further enhances the asymmetry.

1. Introduction

Although track forecasts have improved substantially over recent decades, ongoing development of operational regional coupled tropical cyclone (TC) forecast models such as the Geophysical Fluid Dynamics Laboratory (GFDL) and Hurricane Weather Research and Forecasting (HWRF) systems have not yet produced a commensurate improvement in intensity forecasts. The ocean provides the necessary thermal energy for TCs through moist surface enthalpy flux, but also imposes a negative feedback where increasing wind speed drives

faster SST cooling that opposes intensification. Up to 90% of SST cooling results from shear-driven turbulent entrainment of deeper cold water into the ocean mixed layer (OML; Elsberry et al. 1976; Chang 1979; Price 1981; Shay et al. 1992; Jacob et al. 2000). The resulting impact of the ocean negative feedback therefore depends substantially on the prestorm thickness of the warm surface layer above the seasonal thermocline. The prestorm OML is usually thinner than this warm surface layer so that when a storm strikes, the OML initially entrains relatively warm water and cools slowly. When the prestorm warm layer is thick, substantial time elapses before the OML base reaches the seasonal thermocline to entrain much colder water, and when it does, the large thermal inertia continues to limit the subsequent SST cooling rate. In regions with very thick warm layers such

Corresponding author address: George Halliwell, NOAA/AOML/PhOD, 4301 Rickenbacker Causeway, Miami, FL 33149.
E-mail: george.halliwell@noaa.gov

as the northwestern Caribbean Sea and western boundary current systems (e.g., the Loop Current, Florida Current, and Gulf Stream), cumulative SST cooling is usually <1°C, even for major hurricanes. By contrast, cumulative cooling can reach several degrees Celsius in regions with thin prestorm warm layers.

Tropical cyclone heat potential (TCHP) relative to the 26°C isotherm (Leipper and Volgenau 1972; Shay et al. 2000; Goni and Trinanes 2003; Mainelli et al. 2008; Goni et al. 2009; Lin et al. 2013), often referred to as ocean heat content, is a commonly used index to assess negative feedback strength:

$$\text{TCHP} = c_p \int_0^{D_{26}} \rho[T(z) - 26]\, dz, \qquad (1)$$

where c_p is specific heat at constant pressure and D_{26} is the 26°C isotherm depth. TCHP derived from satellite altimetry is used to improve intensity forecasts in the Statistical Hurricane Intensity Prediction Scheme (SHIPS; DeMaria et al. 2005; Mainelli et al. 2008). Other improved indices have recently been developed that either add stratification effects (Shay and Brewster 2010) or are based on conserved fields such as vertically averaged temperature over the upper 100 m (Price 2009) and potential energy considerations (Vincent et al. 2012). TCHP is analyzed in the present study because of its ongoing operational use.

For cases where the large-scale atmospheric environment is favorable for intensification, the ocean potentially plays a significant role in intensity evolution (e.g., Lloyd and Vecchi 2011). TC intensification (weakening) has been observed for a number of storms as they pass over regions with high (low) TCHP. Intensification associated with the warm Loop Current (LC) and warm-core anti-cyclones in the Gulf of Mexico (GoM) was documented for 1995 Hurricane Opal (Jacob et al. 2000; Hong et al. 2000; Shay et al. 2000; Jacob and Shay 2003), and also for 2005 Hurricanes Katrina and Rita (Scharroo et al. 2005; Sun et al. 2006; Shay 2009; Jaimes and Shay 2009, 2010). Weakening was documented for 2004 Hurricane Ivan (Walker et al. 2005) along with Rita (Sun et al. 2006; Jaimes and Shay 2009, 2010) as they passed over cold-core cyclones in the GoM. Large horizontal TCHP differences in the subtropical western North Pacific region are often associated with typhoon intensity changes (e.g., Lin et al. 2005; Wada and Usui 2007; Wu et al. 2007, 2008; Lin et al. 2008, 2009a,b; Chiang et al. 2011). Oceanic impacts have been demonstrated and analyzed in modeling studies (e.g., Schade and Emanuel 1999; Kim et al. 2014; Ito et al. 2015).

For most storms, unambiguous isolation of the oceanic influence on intensity is difficult or impossible due to the dominant impact of atmospheric processes. Cione

(2015) analyzed surface buoy observations to demonstrate that atmospheric temperature and humidity fluctuations are the predominant mechanism forcing enthalpy flux changes at Northern Hemisphere latitudes <29°N over the open Atlantic where horizontal TCHP variability is relatively small compared to the GoM and western North Pacific. Large-scale atmospheric processes that affect intensity involve the synoptic-scale environment (e.g., wind shear, dry air entrainment, and interaction with midlatitude troughs) while small-scale mechanisms involve dynamical and thermodynamical processes (e.g., convection) in the inner core region of storms (e.g., Emanuel et al. 2004). Even for the storms mentioned above where intensity has been observationally related to along-track TCHP changes, the possibility that atmospheric processes made a significant impact cannot be ruled out. Moreover, we have limited quantitative understanding of the relationship between storm intensity and changes in the rate and pattern of SST cooling. This is particularly true beneath the inner core where cooling has the largest impact on enthalpy flux because adequate observational coverage to analyze the cooling pattern in detail there is not available. We also have limited quantitative understanding of the expected time scales over which storm intensity adjusts when moving from a region of low to high TCHP and vice versa. This time scale in conjunction with storm translation speed determines the minimum horizontal scales of ocean features that potentially have a significant influence on intensity.

To address these questions, TC simulations are performed using an idealized coupled TC forecast model to isolate the oceanic influence on intensity change. Specific foci include 1) determining the dependence of equilibrium intensity on ocean and storm parameters (prestorm TCHP, storm translation speed, storm size); 2) quantifying the magnitude and time scale of intensity adjustment as a storm moves from warmer to colder ocean regions and vice versa as a function of storm parameters; 3) relating the above phenomena to the magnitude and pattern of SST cooling and associated enthalpy flux change, particularly in the inner-core region; and 4) determining the joint impact of SST cooling and atmospheric feedback mechanisms on the enthalpy flux change. The primary intent is not to document the dependence of the oceanic influence on storm parameters per se because these impacts are broadly understood, such as the increasing oceanic influence on intensity change associated with decreasing translation speed (e.g., Schade and Emanuel 1999; Lin et al. 2009a,b; Mei et al. 2012). Instead, the intent is to quantitatively document the sensitivity of a specific atmospheric model that is used operationally to SST

cooling beneath storms under conditions where large-scale atmospheric processes do not force intensity changes. Although atmospheric forcing is minimized, atmospheric feedbacks in response to SST change still affect intensity through adjustments in 10-m wind speed along with 10-m temperature and humidity. Consequently, the present analysis of mechanisms that control storm intensity in this idealized framework focuses on the coupled ocean–atmosphere physical processes that control enthalpy flux from ocean to atmosphere.

The idealized coupled forecast system is described in section 2 while the experimental setup is described in section 3. The impact of oceanic cooling on quasi-equilibrium storm intensity under constant oceanic conditions is described as a function of storm parameters and oceanic conditions in section 4. Section 5 describes the magnitude and time scale of intensity change in response to changing TCHP as a function of storm parameters. Results and conclusions are summarized in section 6.

2. The idealized coupled forecast model

a. Atmospheric model

Gopalakrishnan et al. (2011) used an uncoupled research version of the operational HWRF model to perform an idealized study of TC intensification. An initial bogus vortex was embedded in uniform easterly $4\,\mathrm{m\,s^{-1}}$ trade winds on double-nested (27 and 9 km) f-plane grids. Given that an uncoupled model was used, that study focused entirely on atmospheric processes responsible for intensification. Gopalakrishnan et al. (2013) then used a later version of this atmospheric model, specifically the triply nested HWRFV3.2, to study the impact of vertical diffusion on the intensity and structure of tropical cyclones. That model was also used by Bao et al. (2012) to study the impact of boundary layer and physics parameterizations on the intensification of an idealized vortex. HWRFV3.2 was configured with a coarse mesh parent domain of 27-km horizontal grid spacing covering about $50° \times 50°$ and two two-way telescopic moving nests, one with 9-km resolution covering about $15° \times 15°$ and the other with 3-km resolution covering about $5° \times 5°$. The system of equations is formulated on a rotated latitude/longitude Arakawa E grid and on vertical pressure-sigma hybrid coordinates. There are 42 hybrid levels with at least 11 located below 850 hPa. The model contains essentially the same Nonhydrostatic Mesoscale Model (NMM) dynamical core used operationally at the NOAA/ National Centers for Environmental Prediction (NCEP) prior to 2013. Procedures for coupling the moving nests

to the parent domain and to each other are described in Gopalakrishnan et al. (2011).

b. The one-dimensional ocean model

These prior studies are extended herein by coupling HWRFV3.2 to a one-dimensional ocean model. The one-dimensional momentum and scalar equations solved by the model are

$$\frac{\partial u}{\partial t} = fu + \frac{\partial}{\partial z}\left(K_M \frac{\partial u}{\partial z}\right),$$
$$\frac{\partial v}{\partial t} = -fv + \frac{\partial}{\partial z}\left(K_M \frac{\partial v}{\partial z}\right), \tag{2}$$

and

$$\frac{\partial T}{\partial t} = \frac{\partial}{\partial z}\left(K_S \frac{\partial T}{\partial z}\right),$$
$$\frac{\partial S}{\partial t} = \frac{\partial}{\partial z}\left(K_S \frac{\partial S}{\partial z}\right), \tag{3}$$

where K_M is the vertical viscosity coefficient and K_S is the scalar diffusion coefficient. These equations are closed by the K-profile parameterization (KPP) vertical mixing model (Large et al. 1994) to estimate K_M and K_S, and by an equation of state to update density that is third order in temperature and second order in salinity. Code to solve these equations was extracted from the Hybrid Coordinate Ocean Model (HYCOM; Bleck 2002; Halliwell 2004; Chassignet et al. 2007). This ocean general circulation model has been coupled to the HWRF atmospheric model and this coupled system is now undergoing pre-operational tests at the NOAA/Environmental Modeling Center (EMC). Extraction of this code directly from HYCOM will facilitate planned comparisons between models coupled to a one-dimensional and three-dimensional ocean. Surface boundary conditions required by these equations are provided by the atmospheric model, directly for momentum flux and through bulk formulas for the latent and sensible components of the enthalpy flux where the atmospheric model provides the required 10-m wind speed, atmospheric temperature, and atmospheric humidity. For mass flux, precipitation is provided by the atmospheric model while evaporation is calculated using a bulk formula.

The one-dimensional ocean model is included in HWRFV3.2 as a module containing subroutines used by both the initialization and solver components that are called separately at all grid points on all three nests. All that is asked of the ocean model in the present study is to produce an SST cooling response with a realistic magnitude and pattern with respect to the idealized

a) Schematic of Idealized Ocean Domain

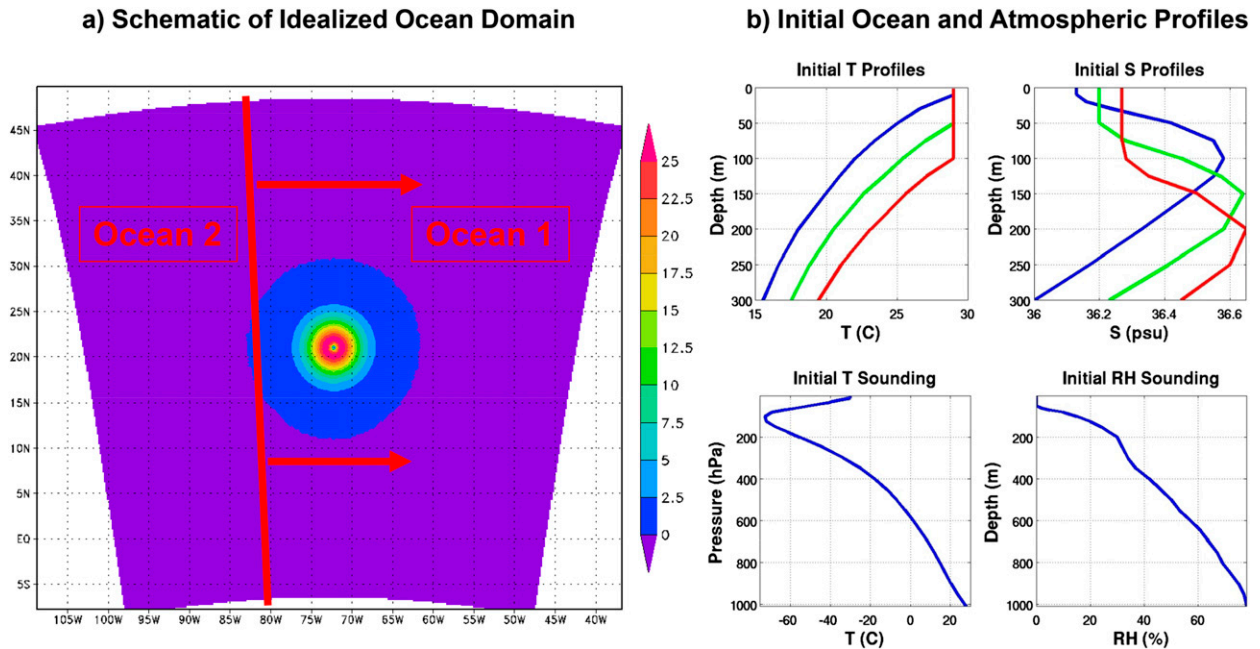## b) Initial Ocean and Atmospheric Profiles

FIG. 1. (a) Schematic representation of the idealized initial atmosphere and ocean on the model parent domain. Colors show wind speed with the initial vortex situated at the center of the domain. The ocean is divided into two regions with ''ocean 1'' representing the initial state and ''ocean 2'' representing the alternate state eventually encountered by the storm as ocean fields are advected eastward. For uniform ocean experiments, both regions are initialized with the same state. (b) Initial oceanic and atmospheric profiles. Initial temperature and salinity profiles represent three oceanic states: cool (blue), warm (green), and hot (red). The initial temperature and humidity sounding was used to initialize the horizontally uniform unperturbed atmosphere away from the initial vortex.

storms. Although it will be demonstrated that the ocean model does reproduce cold wakes with realistic magnitudes that are displaced to the right of the storm track as observed, missing ocean dynamics do affect the results presented herein. These limitations are considered in the analysis design and in the interpretation of results. This study must be considered as a first step toward isolating and understanding the impact of ocean–atmosphere coupling on TC intensity evolution forced almost entirely by changes in SST cooling. Because of the ocean model limitations, physics-based evaluation of the ocean model response is not conducted.

3. Experiments

The overarching strategy is to initialize the simplest possible atmosphere and ocean that permits storm intensity to be controlled almost entirely by SST cooling but that still permits feedback in response to the cooling. Each experiment is initialized with a bogus vortex possessing properties highly favorable for intensification as in Gopalakrishnan et al. (2011, 2013) that is embedded within a horizontally homogeneous atmosphere. With the far-field atmosphere at rest, the storms remain approximately stationary during the forecasts. The impact of storm motion on the ocean response must therefore

be introduced by bodily advecting the underlying ocean fields at a prespecified velocity.

a. Idealized representation of the atmosphere

The fixed curvilinear parent grid centered at 21.0°N, 72.5°W maintains a relatively uniform grid size as a function of latitude, resulting in a longitudinal extent that increases from ~50° at the southern end to ~75° at the northern end (Fig. 1a). No land is present. The f-plane atmosphere is initialized in a state of rest using horizontally uniform initial profiles characteristic of the tropical North Atlantic during the height of TC season (Fig. 1b). For each experiment, an initial bogus vortex (Fig. 1a) is embedded following the procedure used by Gopalakrishnan et al. (2011, 2013) in the exact center of the parent domain (21.0°N, 72.5°W). The two moving nests are initially situated so that this vortex is approximately centered within them. In this idealized scenario, the evolving storm is able to draw upon an essentially infinite supply of deep tropical moisture from the far-field atmosphere in a zero-shear environment. SST cooling is the only significant large-scale mechanism limiting intensity in this highly favorable environment that would otherwise allow storms to approach maximum possible intensity (Miller 1958; Emanuel 1988; Holland 1997; Emanuel et al. 2004).

b. Idealized representation of the ocean

The initial ocean fields used for each forecast are horizontally uniform and are based on profiles of temperature (Fig. 1b) that represent TCHP values of 27 kJ cm^{-2} ("cool ocean"), 85 kJ cm^{-2} ("warm ocean"), and 148 kJ cm^{-2} ("hot ocean"). The hot ocean case is characteristic of the warmest parts of the Atlantic hurricane region, such as the northwest Caribbean Sea and the Loop Current in the GoM. The cool ocean case is characteristic of regions inshore of the Atlantic western boundary current, which includes the Gulf common water of the interior northern and central GoM. The warm ocean case is characteristic of large parts of the western Atlantic warm pool region at the height of TC season. The three corresponding salinity profiles display the subsurface maximum characteristic of the subtropical North Atlantic.

Two categories of ocean experiments are run. The first set of "uniform ocean" experiments is initialized with oceans that are horizontally uniform throughout the entire parent domain. The second set of "dual-ocean" experiments is initialized as shown in Fig. 1a. The storm completes its initial rapid intensification over ocean region 1, and then encounters different ocean conditions as the meridional boundary separating the two regions passes beneath the storm. For each experiment the meridional boundary is initially located along a zonal grid point chosen such that the boundary passes beneath the storm center at approximately forecast hour 60. Timing errors due to storm wobbling are always less than ± 2 h. With a one-dimensional ocean model, geostrophic adjustment does not occur along the boundary and the ocean remains at rest.

The eastward advection of ocean fields that accounts for storm motion is introduced as follows: First, propagation distance $v_T t$, where v_T is the prescribed storm translation speed and t is the accumulated model run time, is calculated during each time step of the model run. Whenever the function $v_T t / \Delta x$, where Δx is the zonal grid resolution, crosses an integer value, ocean fields at each grid point (i, j) at all depths are replaced by fields at grid point $(i - 1, j)$, starting from the eastern edge of the domain and working westward. This discrete advection procedure is executed separately on each grid. Fields at the western edge of the parent domain are held constant at the initial profile values. Fields at the western edge of the 9-km moving nest are interpolated from the parent domain while fields at the western edge of the 3-km nest are interpolated from the 9-km nest. Given that the parent domain and both moving nests reside on a curvilinear mesh, the zonal separation distance Δx is determined at the domain center of the parent domain and at the center of each moving nest. Although the time interval separating execution of this advection procedure on the innermost 3-km grid is substantially longer than the model update time step, a realistically smooth SST cooling pattern is still generated.

Although the idealized ocean is initially at rest, the missing dynamics of a one-dimensional ocean model will still affect the forecast SST. The response to storms translating faster than the first-mode baroclinic Rossby wave phase speed consists of a forced near-inertial wave wake (e.g., Greatbatch 1984). The downward group velocity of near-inertial waves reduces kinetic energy in the OML, resulting in reduced shear and cold water entrainment at the base. With a one-dimensional ocean model, however, a storm forces a nonspreading wake of pure inertial oscillations. Without downward energy propagation, the energy of forced currents is trapped within the OML and the stronger currents increase shear and entrainment at the OML base. Another problem is the absence of upwelling and downwelling in the one-dimensional ocean model (e.g., Greatbatch 1985; Suzuki et al. 2011). This encompasses both the upwelling and downwelling directly forced beneath the storm and the alternating upwelling/downwelling pattern associated with the near-inertial wave wake behind the storm. Yablonsky and Ginis (2009) demonstrated that lack of upwelling produces significant errors in SST cooling for storms that propagate at speeds $<5 \text{ m s}^{-1}$. These potential impacts from ocean model limitations are considered in the subsequent experimental design and in the interpretation of results.

c. Experiments

The chosen configurations of uniform and dual ocean experiments are presented in Tables 1 and 2, respectively. Coupled experiments with six translation speeds (0, 2, 4, 6, 8, and 10 m s^{-1}) along with uncoupled experiments are investigated. Two storm sizes are considered, with size controlled by varying the radius of the initial vortex (Table 3) (Xu and Wang 2010). All idealized forecasts were run for 96 h and model fields on the 3-km innermost mesh were archived hourly for analysis. Preliminary processing of these archived model fields involves remapping them from the native E grid of the atmospheric model onto a radial-cylindrical coordinate system using the Diapost program (Zhang et al. 2011). Two-dimensional model fields are then decomposed into a time-dependent azimuthally averaged function of radius $[\overline{f}(r, t)]$ plus a time-dependent residual function of radius and azimuthal angle $[f'(r, \lambda, t)]$:

$$f(r, \lambda, t) = \overline{f}(r, t) + f'(r, \lambda, t)$$

$$= \frac{1}{2\pi} \int_0^{2\pi} f(r, \Lambda, t) \, d\Lambda + f'(r, \lambda, t), \quad (4)$$

TABLE 1. Naming convention for the uniform ocean experiments that are analyzed, including the two uncoupled experiments. The experiments with $6\,\mathrm{m\,s}^{-1}$ translation speed serve as reference experiments that are analyzed in detail. N/A signifies not applicable.

Initial ocean thermal state	Stationary	$2\,\mathrm{m\,s}^{-1}$	$4\,\mathrm{m\,s}^{-1}$	$6\,\mathrm{m\,s}^{-1}$ (reference speed)	$8\,\mathrm{m\,s}^{-1}$	$10\,\mathrm{m\,s}^{-1}$
Uncoupled (SST = 29°C)	UL00U	N/A	N/A	N/A	N/A	N/A
	US00U					
TCHP = $27\,\mathrm{kJ\,cm}^{-2}$	UL00C	UL02C	UL04C	UL06C	UL08C	UL10C
	US00C	US02C	US04C	US06C	US08C	US10C
TCHP = $85\,\mathrm{kJ\,cm}^{-2}$	UL00W	UL02W	UL04W	UL06W	UL08W	UL10W
	US00W	US02W	US04W	US06W	US08W	US10W
TCHP = $148\,\mathrm{kJ\,cm}^{-2}$	UL00H	UL02H	UL04H	UL06H	UL08H	UL10H
	US00H	US02H	US04H	US06H	US08H	US10H

where Λ is the dummy variable of integration around the azimuthal axis.

Maps of Q_E in this cylindrical coordinate system for uncoupled experiments UL00U and US00U illustrate the typical structure of large and small storms (Figs. 2a,b). Time series of the radius of mean wind (RMW) from all uniform-ocean experiments (Fig. 2c) demonstrate that final storm sizes are always reached prior to forecast hour 24. The rapid intensification to quasi-equilibrium intensity also occurs prior to hour 24 (not shown) during this eyewall contraction. The size difference between large and small storms is maintained through forecast hour 96 (Fig. 2c). The average RMW for small storms is about 14–15 km prior to forecast hour 80, and then increases to about 18 km. The average RMW for large storms increases from about 40 km at forecast hour 24 to 46 km by forecast hour 60, and then increases more slowly to 50 km by forecast hour 96.

4. Uniform ocean experiments

a. Analysis of enthalpy flux difference between experiments

The uniform ocean experiments are designed to first determine HWRF model sensitivity to parameters TCHP, translation speed, and storm size, and then to determine differences in quasi-equilibrium storm intensity and their relationship to surface enthalpy flux. To analyze processes that contribute to the enthalpy flux

TABLE 2. Dual ocean experiments. The experiments with $6\,\mathrm{m\,s}^{-1}$ translation speed serve as reference experiments that are analyzed in detail.

	$2\,\mathrm{m\,s}^{-1}$	$4\,\mathrm{m\,s}^{-1}$	$6\,\mathrm{m\,s}^{-1}$	$8\,\mathrm{m\,s}^{-1}$
Cool to warm ocean	DL02CW	DL04CW	DL06CW	DL08CW
	DS02CW	DS04CW	DS06CW	DS08CW
Cool to hot ocean	DL02CH	DL04CH	DL06CH	DL08CH
	DS02CH	DS04CH	DS06CH	DS08CH
Warm to cool ocean	DL02WC	DL04WC	DL06WC	DL08WC
	DS02WC	DS04WC	DS06WC	DS08WC
Hot to cool ocean	DL02HC	DL04HC	DL06HC	DL08HC
	DS02HC	DS04HC	DS06HC	DS08HC

differences between experiments, the bulk formula used by HWRFV3.2 to calculate enthalpy flux is considered:

$$Q_E = Q_L + Q_S = \rho_a L_v C_k(v_{10})\Delta q + \rho_a c_p C_k(v_{10})\Delta T, \quad (5)$$

where Q_L and Q_S are the latent and sensible components, $\Delta q = q_s - q_{10}$, $\Delta T = T_s - T_{10}$, q_s and q_{10} are surface saturation and 10-m atmospheric specific humidity, T_s and T_{10} are SST and 10-m atmospheric temperature, v_{10} is 10-m wind speed, and c_p is specific heat. The exchange coefficient for enthalpy flux (C_k) is assumed to equal the coefficients of both the latent (C_e) and sensible (C_h) components. It is calculated by the atmospheric model, with values ranging between 1.1×10^{-3} and 1.2×10^{-3} for wind speeds > $10\,\mathrm{m\,s}^{-1}$ (Bao et al. 2012).

The subsequent analyses focus on azimuthally averaged model fields, which for Q_E must consider the impact of nonlinear terms on the right side of Eq. (5). Given an arbitrary function of the product of two model fields that evolve in time on the radial–azimuthal grid $[f(r, \lambda, t) = g(r, \lambda, t)h(r, \lambda, t)]$, the azimuthal average [Eq. (4)] is given by

$$\overline{f}(r,t) = \overline{g}(r,t)\overline{h}(r,t) + \overline{g'(r,\lambda,t)h'(r,\lambda,t)}. \quad (6)$$

Applying this equation to enthalpy flux in Eq. (5) yields

$$\overline{Q_E}(r,t) = \overline{Q_L}(r,t) + \overline{Q_s}(r,t) \approx \rho_a L_v C_k \overline{v_{10}}(r,t)\overline{\Delta q}(r,t) + \rho_a C_k \overline{v_{10}}(r,t)\overline{\Delta T}(r,t). \quad (7)$$

The terms $\overline{v'_{10}\Delta q'}$ and $\overline{v'_{10}\Delta T'}$ are neglected here because they account for <5% of total $\overline{Q_E}$ for all experiments

TABLE 3. Idealized vortex parameters used for initialization.

Parameters	Storm size	
	Small	Large
Initial max wind speed (m s^{-1})	30	30
Initial radius of max wind (km)	50	105

a) Large Storm (UL00U)

b) Small Storm (US00U)
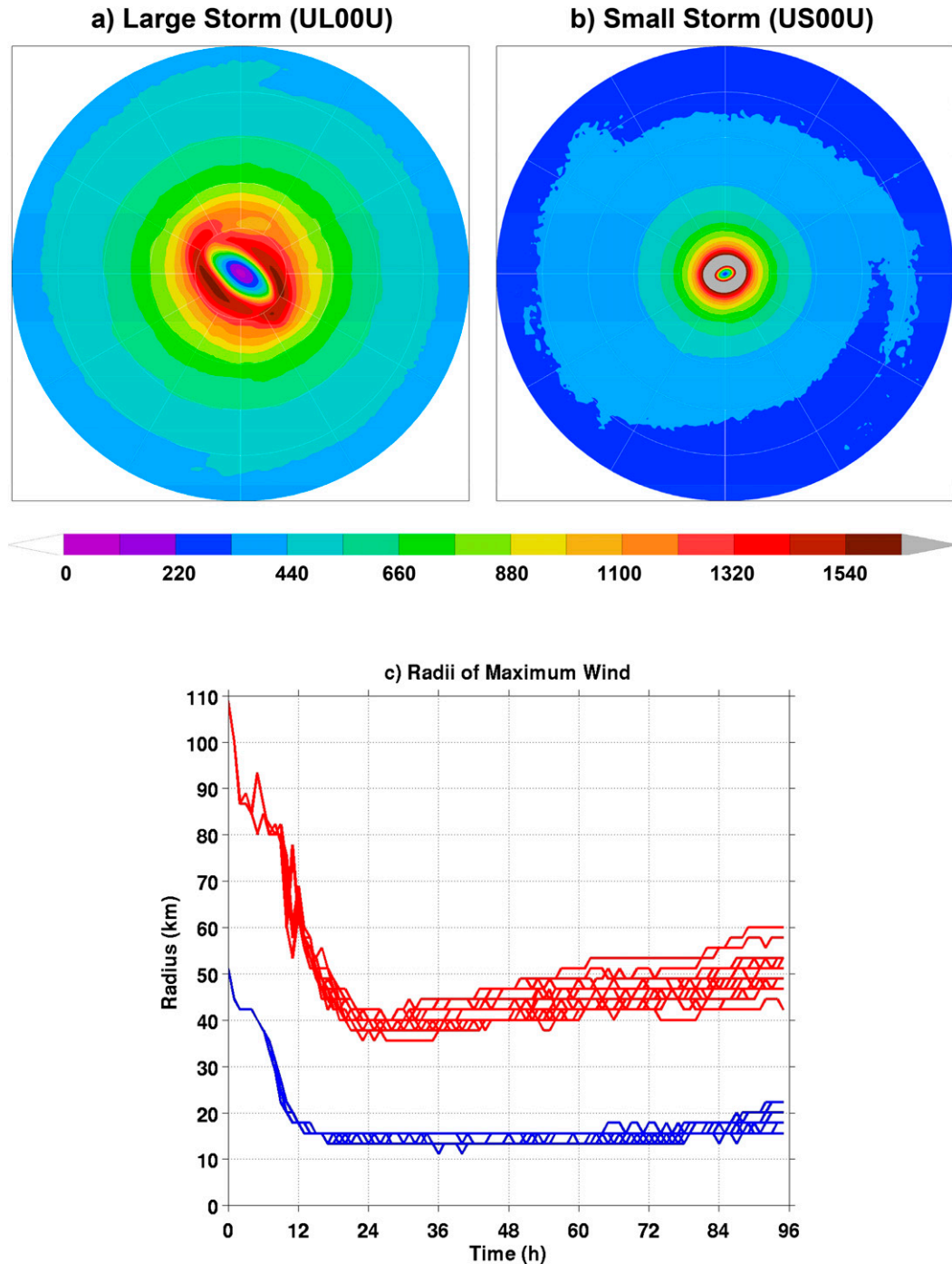
c) Radii of Maximum Wind

FIG. 2. Total enthalpy flux at hour 60 from uncoupled forecasts for (a) large and (b) small storms where SST remains a constant 29°C. The concentric white circles are drawn at intervals of 60 km. (c) Time series of RMW for all large (red) and small (blue) storm experiments. The uncoupled experiment names are given above (a) and (b).

(not shown). Significant correlation does not exist between v_{10} and both $\Delta q'$ and $\Delta T'$, presumably because the former field is dominated by low wavenumber structure around the circumference while the latter fields have their largest amplitudes in the cold wake trailing behind the storm in the right rear quadrant. As a result, differences in $\overline{Q_E}$ between experiments can to lowest order be attributed separately to differences in $\overline{v_{10}}$, $\overline{\Delta q}$, and $\overline{\Delta T}$, and then further attributed to differences in azimuthally averaged atmospheric variables ($\overline{v_{10}}$, $\overline{q_{10}}$, $\overline{T_{10}}$)

TABLE 4. Parameters estimated from the uncoupled experiments for large (UL00U) and small (US00U) storms at forecast hour 60 along with the percentage changes for the small storm with respect to the large storm.

Storm property	Large storms	Small storms	% change, large to small storms
RMW	47 km	15 km	−68
Minimum p	919 hPa	917 hPa	0
$\overline{v_{10}}$ at 1 RMW	59.0 m s^{-1}	67.3 m s^{-1}	14
$\overline{Q_E}$ at 1 RMW	1592 W m^{-2}	2067 W m^{-2}	30
$\overline{Q_L}$ at 1 RMW	1275 W m^{-2} (80% of $\overline{Q_E}$)	1620 W m^{-2} (78% of $\overline{Q_E}$)	27
$\overline{Q_S}$ at 1 RMW	317 W m^{-2} (20% of $\overline{Q_E}$)	447 W m^{-2} (22% of $\overline{Q_E}$)	41
$\overline{q_s}$ at 1 RMW	27.5 g kg^{-1}	27.5 g kg^{-1}	Fixed
$\overline{q_{10}}$ at 1 RMW	21.4 g kg^{-1}	20.5 g kg^{-1}	−5
$\overline{\Delta q}$ at 1 RMW	6.1 g kg^{-1}	7.0 g kg^{-1}	13
$\overline{T_s}$ at 1 RMW	29.0°C	29.0°C	Fixed
$\overline{T_{10}}$ at 1 RMW	25.2°C	24.2°C	−4
$\overline{\Delta T}$ at 1 RMW	3.8°C	4.8°C	26

and oceanic variables ($\overline{q_s}$ and $\overline{T_s}$) to assess the relative contributions of ocean and atmosphere.

b. Uncoupled experiments

The uncoupled experiments UL00U and US00U (Fig. 2) provide baselines for determining the impact of SST cooling on enthalpy flux and storm intensity. Storm properties at forecast hour 60, about 1.5 days after rapid intensification is completed, are summarized in Table 4. Both have very similar minimum central pressures (p_{min}) of 919 and 917 hPa, respectively. By contrast, intensity as measured by maximum $\overline{v_{10}}$ is 14% larger (67.3 vs 59.0 m s^{-1}) for the small storm. At $r = 1$ RMW, $\overline{Q_E}$ is ~30% larger for the small storm (2067 W m^{-2}) than for the large one (1562 W m^{-2}). The corresponding percentage increases in small storms compared to large ones for the latent and sensible components are 27% and 41%, respectively. The latent heat component accounts for 78% of total $\overline{Q_E}$ for the small storm and 80% for the large storm. From Eq. (7), the ~30% larger maximum $\overline{Q_E}$ in the small storm results from changes in each of $\overline{v_{10}}$, $\overline{\Delta q}$, and $\overline{\Delta T}$, which are 14%, 13%, and 26% larger, respectively (Table 4). Given that $\overline{q_s}$ and $\overline{T_s}$ are fixed in these uncoupled experiments, the contributions of $\overline{\Delta q}$ and $\overline{\Delta T}$ to the larger enthalpy flux result from a smaller value of $\overline{q_{10}}$ (20.5 vs 21.4 g kg^{-1}) and cooler $\overline{T_{10}}$ (24.2° vs 25.2°C) in the small storm. In addition to slower wind speed, maximum $\overline{Q_E}$ is reduced in the large storm because the atmospheric boundary layer inflow becomes warmer and more humid by the time that air parcels reach the eyewall.

c. Ocean model performance

Ocean model realism is assessed primarily by the structure of the cold wake and the maximum SST cooling within it. To assess the realism of the cold wake produced by the one-dimensional ocean model at forecast hour 60, both SST and enthalpy flux are mapped in

cylindrical coordinates for both large and small storms translating over a warm ocean (TCHP = 85 kJ cm^{-2}) at 2, 4, and 8 m s^{-1} (Fig. 3). In all cases, the ocean model produces a qualitatively realistic cold wake structure displaced to the right of the storm track, with large storms producing greater cooling than small ones. Maximum cooling typically occurs in the right rear quadrant between 3 and 5 RMW from the storm center. Maximum cooling ranges from 4.3°C for the large storm translating at 2 m s^{-1} (experiment UL02W) to 0.8°C for the small storm translating at 8 m s^{-1} (experiment US08W), roughly consistent with observed values. In the four cases in Fig. 3 where translation speed equals or exceeds 4 m s^{-1}, cooling within 2 RMW of storm center averages <1°C, roughly consistent with the results of Cione and Uhlhorn (2003). However, limited availability of observations beneath the inner core does not permit detailed analysis of the cooling structure in this region. Although the SST cooling pattern is affected by the absence of upwelling and downwelling in the ocean model, particularly for slower translation speeds (Yablonsky and Ginis 2009), their overall structure and magnitude retain sufficient realism to justify use of the one-dimensional ocean model in this initial idealized study of the oceanic impact on HWRF.

d. Parameter dependence of quasi-equilibrium intensity

The dependence of quasi-equilibrium storm intensity produced by the model on parameters TCHP, translation speed, and storm size is analyzed first. Schade and Emanuel (1999) performed a detailed analysis of the sensitivity of an axisymmetric coupled model to seven different oceanic and atmospheric parameters including the three analyzed herein. The intent of the present analysis is neither to reproduce this earlier analysis, which required a very large number of experiments, nor

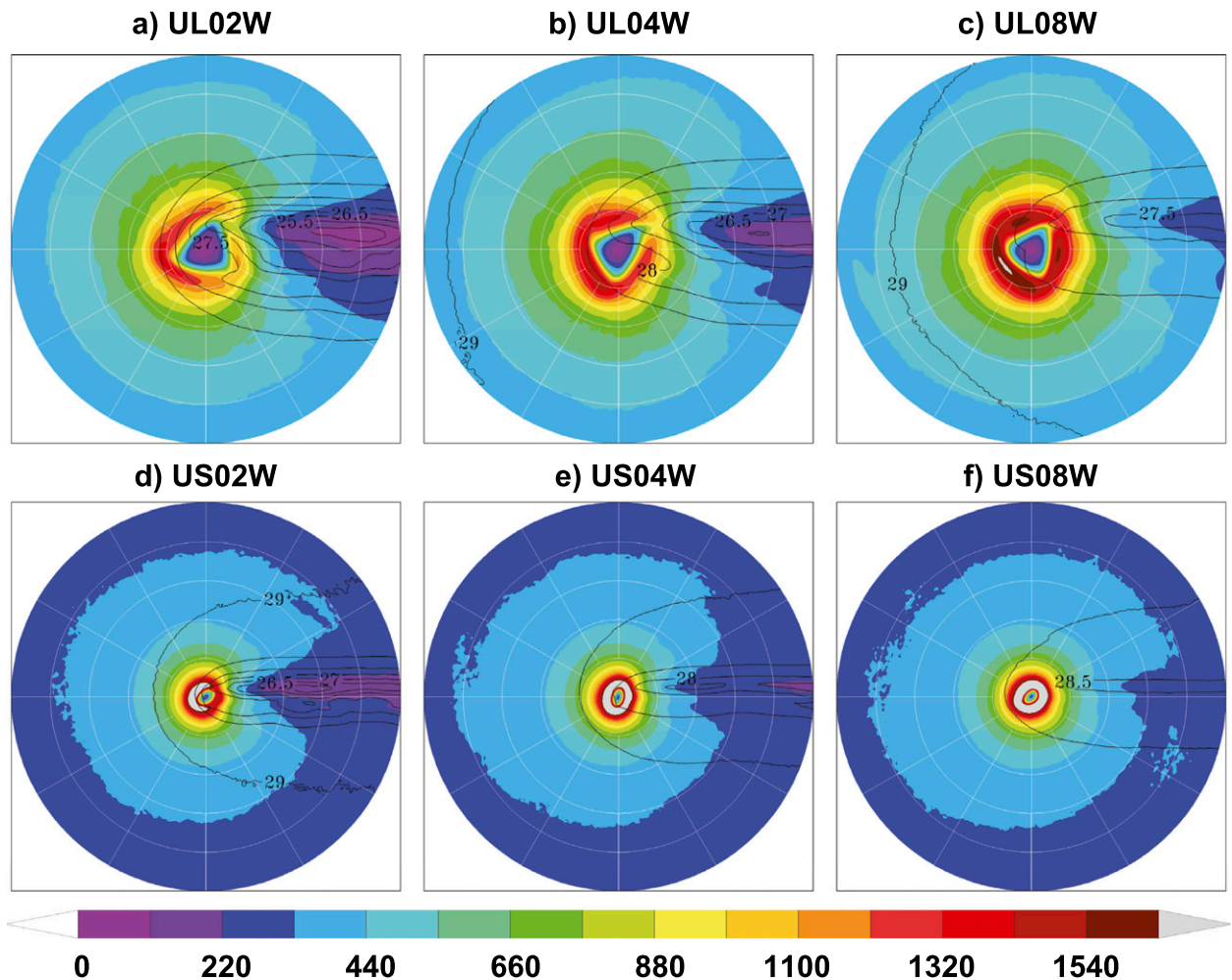## a) UL02W   b) UL04W   c) UL08W

d) US02W   e) US04W   f) US08W

FIG. 3. Total enthalpy flux at hour 60 with SST contours overlaid for six uniform-ocean forecasts initialized with warm ocean conditions. (top) Large storms with translation speeds of (a) 2, (b) 4, and (c) 8 m s^{-1}. (bottom) Small storms with translation speeds of (d) 2, (e) 4, and (f) 8 m s^{-1}. In all panels, SST is contoured at 0.5°C intervals. Experiment names (Table 1) are given above each panel.

to accurately reproduce the actual TC sensitivity to SST cooling that exists in nature. Instead, the intent is to document and understand model sensitivity to SST over a broad range of cooling rates. To include large cooling cases, the impact of storm translation speed is extended to stationary storms.

Intensity at hour 60 as represented by minimum central pressure (p_{min}) and maximum $\overline{v_{10}}$ is contoured separately for large and small storms as a function of TCHP and translation speed (Fig. 4). The model intensity forecasts demonstrate the expected dependence on these parameters, with reduced sensitivity to the ocean experienced by faster-moving storms and by storms moving over regions with larger values of TCHP where ocean cooling is relatively small. Large storms are substantially more sensitive to the ocean in comparison to small storms throughout this parameter space (Fig. 4). For all storms, intensity is substantially more sensitive to

TCHP than to translation speed, particularly for TCHP values <85 kJ cm^{-2}, with the exception of small storms translating at <2 m s^{-1}. For TCHP values ≥85 kJ cm^{-2}, sensitivity to the ocean is relatively weak for large storms and essentially nonexistent for small storms translating at ≥2 m s^{-1}. This weak impact on intensity for large TCHP is associated with a relatively weak sensitivity of maximum $\overline{Q_E}$ to both TCHP and translation speed due to slow SST cooling (Fig. 5). Schade and Emanuel (1999) related storm intensity to translation speed and mixed layer thickness, determining approximately equal sensitivity to both of these parameters. Differences from the present results are due to the use of mixed layer thickness instead of TCHP, and use of a different coupled model.

By contrast to other ocean fields, maximum SST cooling is about equally sensitive to TCHP and storm translation speed, and it also remains sensitive to both TCHP and translation speed at large TCHP values
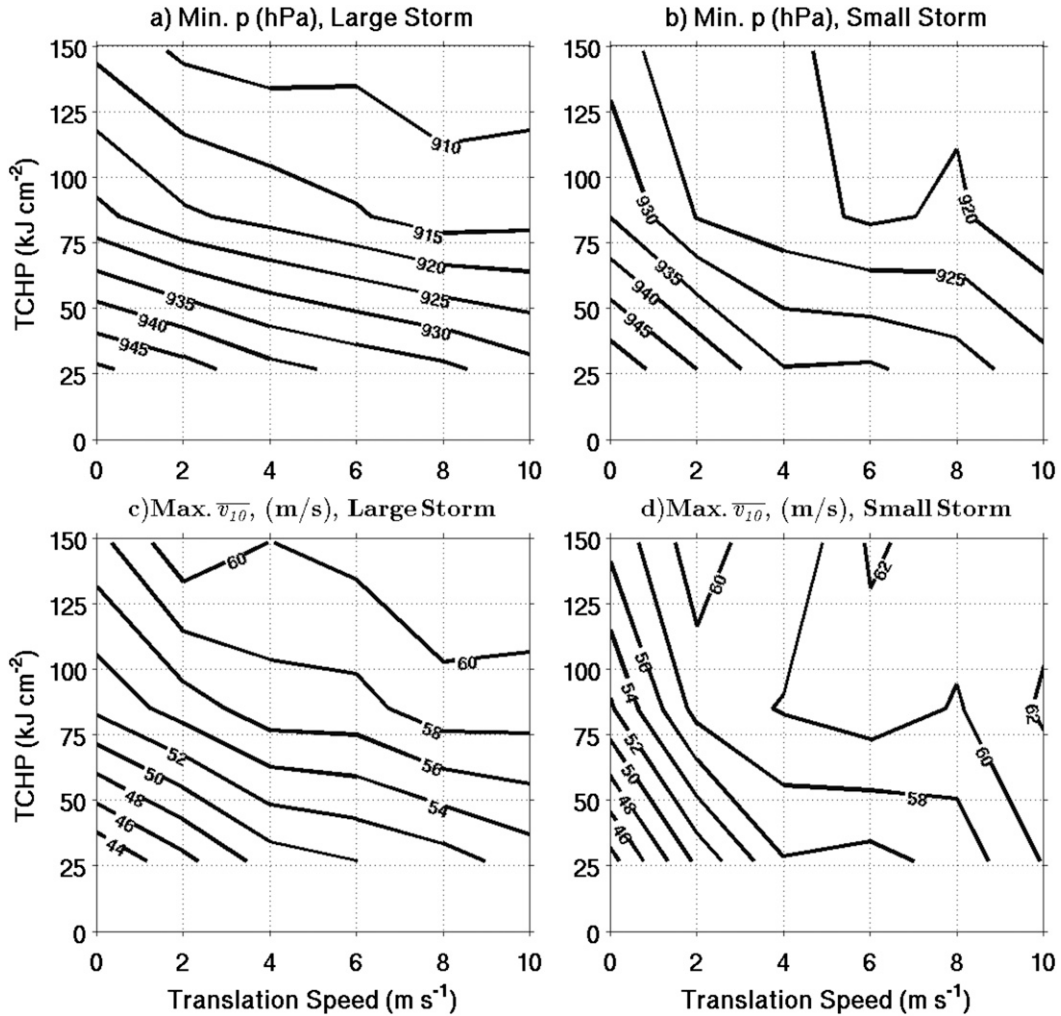
FIG. 4. Minimum central pressure for (a) large and (b) small storms, and maximum $\overline{v_{10}}$ for (c) large and (d) small storms, averaged over forecast hours 72–96.

(Fig. 5), consistent with results of Schade and Emanuel (1999). This sensitivity in maximum SST cooling at large TCHP does not translate to sensitivity in storm intensity, presumably because maximum cooling occurs in the cold wake behind the storm while it is cooling beneath the inner core region, particularly in the eyewall, that has the greatest impact on intensity (Cione and Uhlhorn 2003).

The intensity contours in Fig. 4 reveal that for stationary storms, intensity remains strong at hour 60. Despite SST cooling beneath the eyewall to ~22°C in UL00C and to ~22.5°C in US00C that greatly reduces $\overline{Q_E}$, hurricane-force winds are maintained through hour 96. It is likely that the unlimited far-field deep tropical moisture available to the storm in this idealized setting also contributes significantly to maintaining the storm and continues to provide significant enthalpy to the storm even with $\overline{Q_E}$ greatly reduced. It is possible that the sensitivity of the atmospheric model to ocean cooling

reported here would be larger if the far-field source of high-enthalpy air was reduced. Investigation of this hypothesis is beyond the scope of this paper.

Sensitivity to inner-core SST cooling is analyzed by comparing scatterplots of p_{min} and maximum $\overline{v_{10}}(r)$ at forecast hour 60 to variables $\overline{T_s}(r)$ and $\overline{Q_E}(r)$ averaged over the interval $r \leq 3$ RMW. Stationary storms are omitted from this analysis. For both large and small storms, intensity as represented by both minimum pressure and maximum $\overline{v_{10}}$ has an approximately linear dependence on radially averaged $\overline{Q_E}$ (Figs. 6a,b) and $\overline{T_s}$ (Figs. 6c,d). It is possible to separate the points plotted in Fig. 6 into values obtained from cool, warm, and hot ocean experiments. Based on this separation, radially averaged $\overline{Q_E}$ for small storms is insensitive to storm translation speed for larger TCHP values. Cooling of radially averaged $\overline{T_s}$ never exceeds 1°C for the warm and hot ocean experiments, while it ranges from 1° to 2.6°C
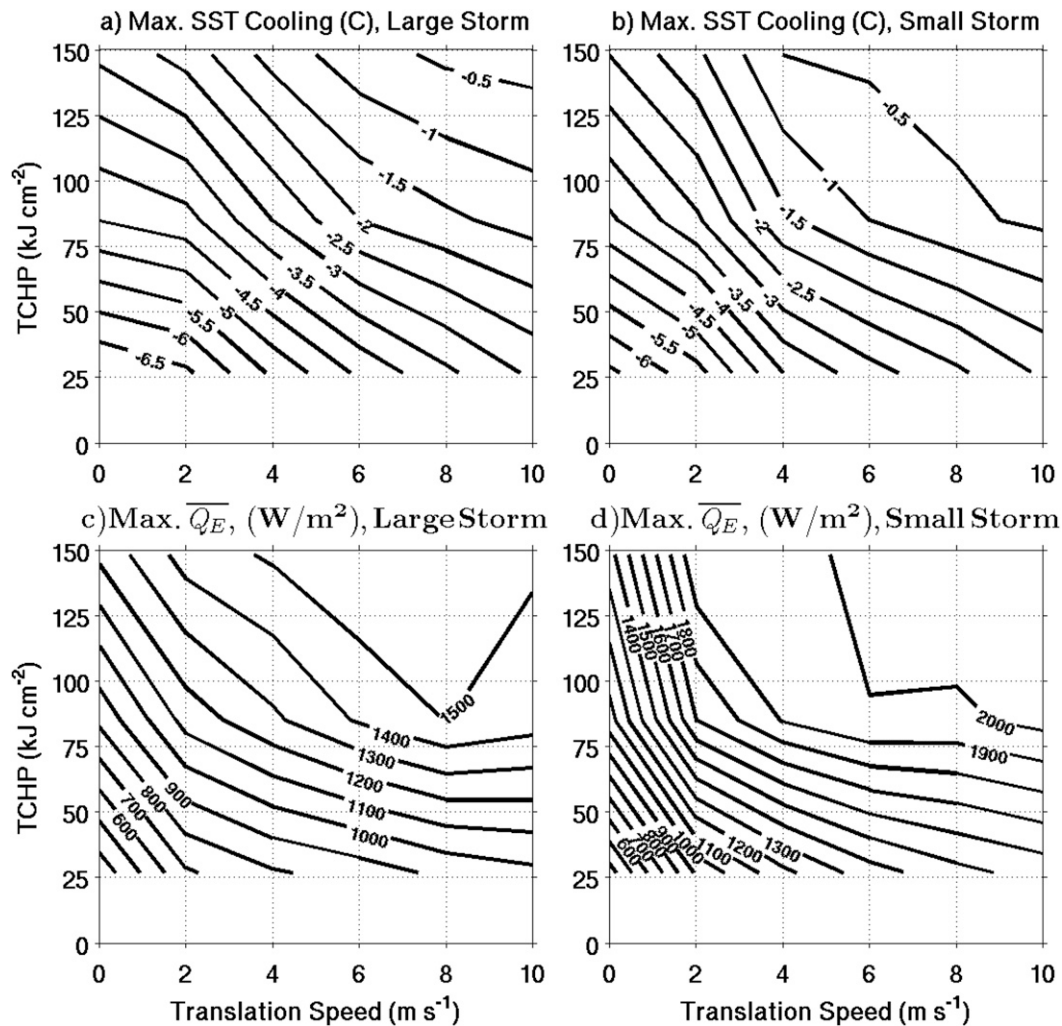
FIG. 5. Maximum SST cooling for (a) large and (b) small storms, and maximum $\overline{Q_E}$ for (c) large and (d) small storms at forecast hour 60, all contoured as a function of storm translation speed and TCHP.

for the cool ocean experiments. The limited cooling in all of the warm and hot ocean experiments leads to radially averaged $\overline{Q_E}$ values that are little changed, again demonstrating the relatively weak ocean influence when TCHP is large.

e. Enthalpy flux analysis

The contribution of enthalpy flux to observed intensity differences among experiments is analyzed by plotting $\overline{Q_E}(r, t)$ from Eq. (7) at forecast hour 60. The impact of TCHP on $\overline{Q_E}(r, 60)$ is examined for large storms in Fig. 7 from experiments UL06H, UL06W, and UL06C and for small storms in Fig. 8 from experiments US06H, US06W, and US06C. This analysis along with all subsequent analyses of enthalpy fluxes are performed only for storms translating at $6\,\mathrm{m\,s^{-1}}$, which is close to the average observed speed of $5.5\,\mathrm{m\,s^{-1}}$, because they

are minimally impacted by the lack of upwelling (Yablonsky and Ginis 2009). Results for storms moving at this speed tend to be representative of results for storms traveling at different speeds (not shown), with the primary impact of speed being a stronger (weaker) ocean influence for slower (faster) storms as expected.

The largest values of $\overline{Q_E}$ at forecast hour 60 occur for hot ocean cases UL06H and US06H (Figs. 7a, 8a), and they are very close to values from the unconstrained experiments UL00U and US00U at all radii. (cf. the maximum values at 1 RMW in Figs. 7a and 8a to values from the unconstrained experiments listed in Table 4). Experiment UL06W produces an ~10% reduction in $\overline{Q_E}$ within the eyewall while US06W produces almost no reduction. Experiment US06C produces an ~50% reduction in $\overline{Q_E}$ while US06C produces only an ~10% reduction. For both large and small storms, there is little
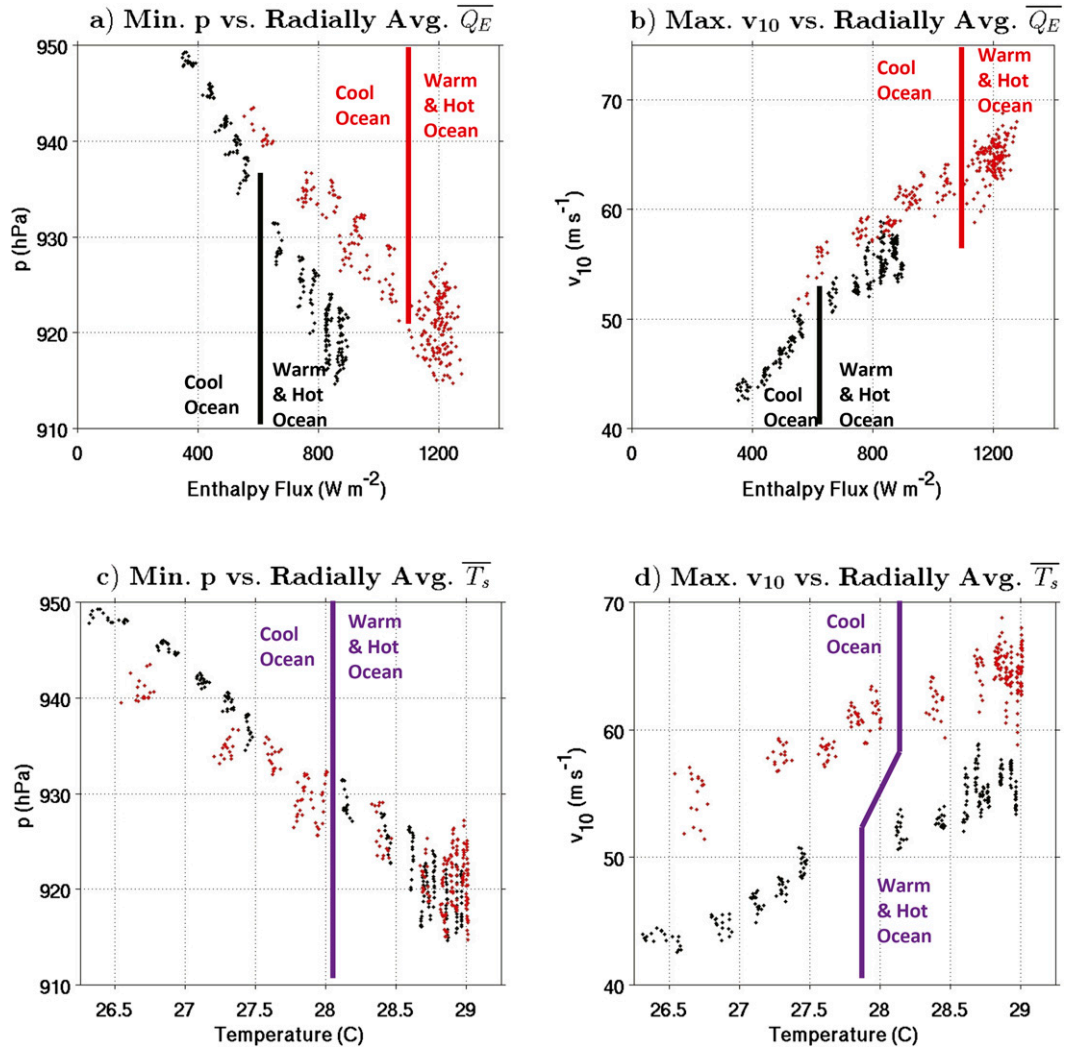
FIG. 6. Scatterplots of storm intensity vs enthalpy flux. (a) Minimum p vs $\overline{Q_E}$ radially averaged over $r < 3$ RMW, (b) maximum v_{10} vs $\overline{Q_E}$ radially averaged over $r < 3$ RMW, (c) minimum p vs $\overline{T_s}$ radially averaged over $r < 3$ RMW, and (d) maximum v_{10} vs $\overline{T_s}$ radially averaged over $r < 3$ RMW. Red (black) points represent small (large) storm experiments. Vertical lines separate cool ocean experiments from both warm and hot ocean experiments. In (a) and (b), the red (black) lines perform this separation for small (large) storms.

change in $\overline{v_{10}}$ in the eyewall between the hot and warm ocean experiments (Figs. 7b, 8b). By contrast, there is an ~21% (~8%) reduction in $\overline{v_{10}}$ in the eyewall between hot and cool ocean experiments for the large (small) storms. The weaker ocean influence on small storms is clearly evident as is the relatively weak impact of TCHP differences between the warm and hot ocean experiments.

Factors other than $\overline{v_{10}}$ that affect $\overline{Q_E}$ are examined by graphing variables $\overline{\Delta q}, \overline{q_{10}}, \overline{q_s}, \overline{\Delta T}, \overline{T_{10}}$, and $\overline{T_s}$ at forecast hour 60 for large (Figs. 7c–f) and small (Figs. 8c–f) storms. For the hot ocean experiments (UL06H and US06H), all six of these variables very closely resemble those from the uncoupled experiments UL00U and US00U (not shown). Before considering the warm and

cool ocean experiments, it is first noted that $\overline{T_s}$ has a different radial structure that might be inferred from the two-dimensional cold wake structure where minimum temperature is encountered several RMW behind the storm. Instead, $\overline{T_s}$ is coldest within 1 RMW of the center, and then monotonically increases with increasing radius as the cold wake covers a decreasing fraction of storm circumference. The radial magnitude and structure of these fields agree well with results from the observational synthesis of Cione et al. (2013).

For experiment UL06W (Fig. 7), there are small decreases in $\overline{q_s}$ and $\overline{T_s}$ at forecast hour 60 compared to UL06H, but little change in $\overline{q_{10}}$ and $\overline{T_{10}}$, which together results in small decreases in $\overline{\Delta q}$ and $\overline{\Delta T}$, and hence in
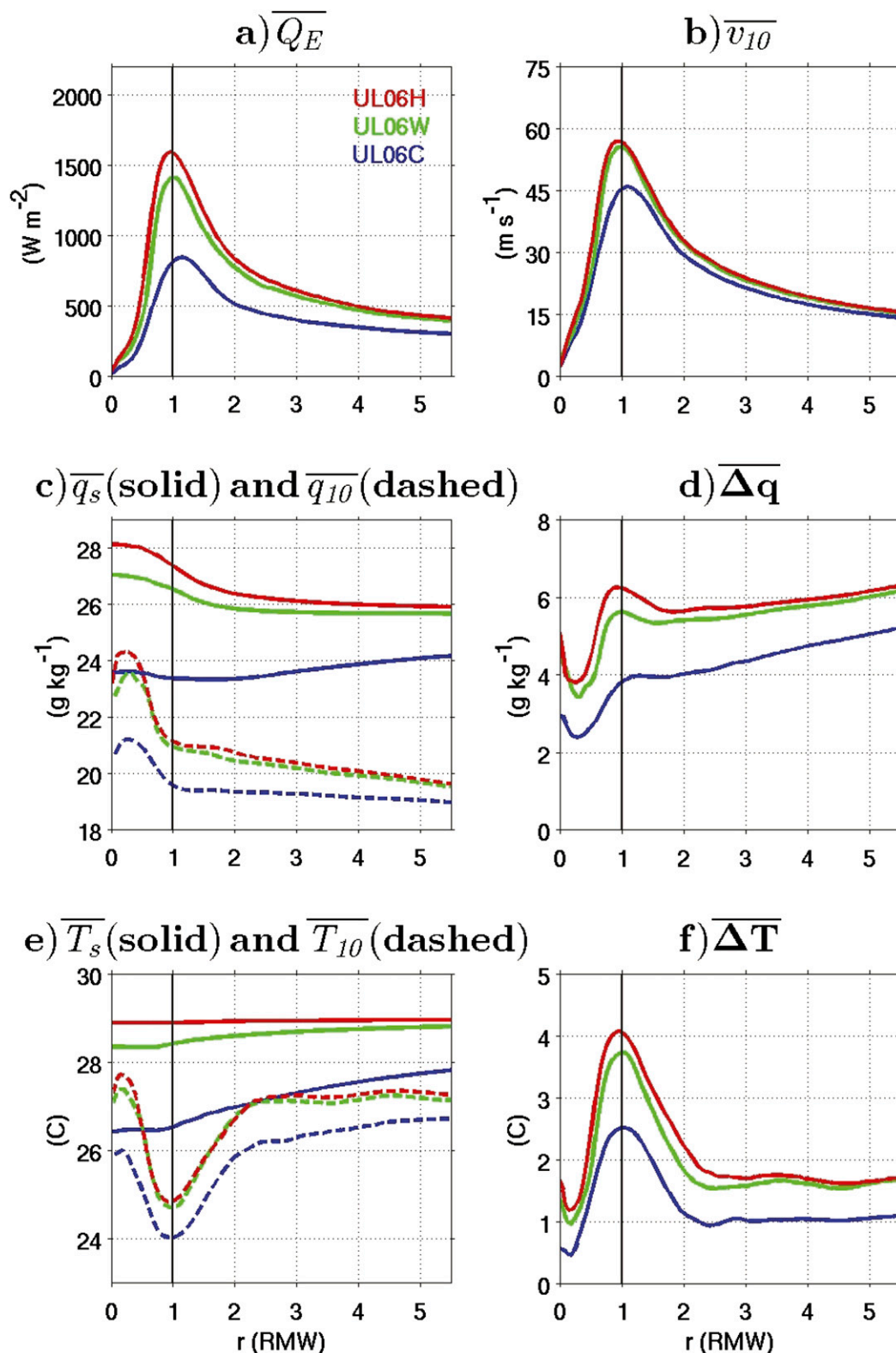
FIG. 7. Analysis of differences in $\overline{Q_E}(r, 60)$ as a function of r for cool (blue), warm (green), and hot (red) ocean experiments for large storms traveling at $6 \, \mathrm{m\,s^{-1}}$: (a) $\overline{Q_E}(r, 60)$, (b) $\overline{v_{10}}(r, 60)$, (c) $\overline{q_s}(r, 60)$ (solid) and $\overline{q_{10}}(r, 60)$ (dashed), (d) $\overline{\Delta q}(r, 60)$, (e) $\overline{T_s}(r, 60)$ (solid) and $\overline{T_{10}}(r, 60)$ (dashed), and (f) $\overline{\Delta T}(r, 60)$. The legend in (a) identifies the experiments. The average RMW for all large storms was used to rescale the x axes.
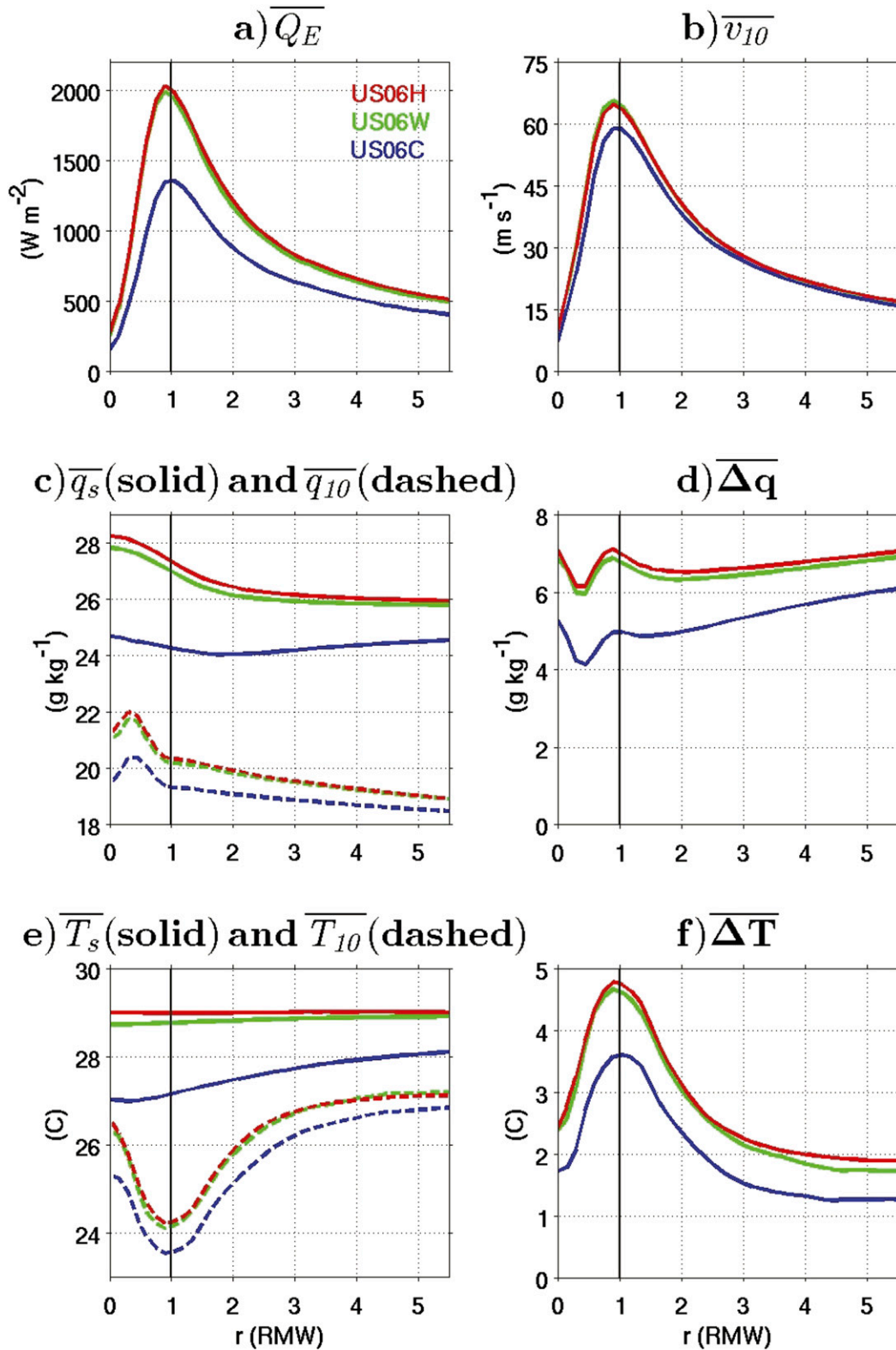
FIG. 8. As in Fig. 7, but for small storms.

$\overline{Q_E}$. For experiment UL06C, there are large decreases in $\overline{q_s}$ and $\overline{T_s}$, and somewhat smaller decreases in $\overline{q_{10}}$ and $\overline{T_{10}}$, which together result in substantial reductions in both $\overline{\Delta q}$ and $\overline{\Delta T}$, and hence in $\overline{Q_E}$. The corresponding results from the small storm experiments (Fig. 8) are generally similar but smaller in magnitude, revealing the lower sensitivity of small storms to the ocean response.

For both large and small storms, the primary contribution of atmospheric variables $\overline{q_{10}}$ and $\overline{T_{10}}$ at forecast hour 60 is to partly compensate for the differences in oceanic variables $\overline{q_s}$ and $\overline{T_s}$ among the cool, warm, and hot ocean experiments. For both size storms, differences in $\overline{q_{10}}$ and $\overline{T_{10}}$ act to reduce the differences in $\overline{\Delta q}$ and $\overline{\Delta T}$, and hence in $\overline{Q_E}$, between warm and cool ocean conditions that would otherwise occur by up to 40%. Ocean sensitivity is too weak to quantify the impact of atmospheric feedback between warm and hot ocean conditions. In this idealized setting, the atmospheric planetary boundary layer primarily provides feedback through temperature and humidity adjustments that reduce enthalpy flux differences produced by the different SST cooling rates. This in turn reduces differences in quasi-equilibrium intensity resulting from differences in prestorm TCHP.

5. Ocean transition experiments

a. Wind speed and enthalpy flux adjustments

Changes in selected model fields after forecast hour 54, specifically $\overline{v_{10}}(r, t) - \overline{v_{10}}(r, 54)$, $\overline{Q_L}(r, t) - \overline{Q_L}(r, 54)$, and $\overline{Q_s}(r, t) - \overline{Q_s}(r, 54)$, are presented in Hovmöller diagrams for the dual ocean experiments DL06CH, DS06CH, DL06HC, and DS06HC, again limited to storms translating at $6\,\mathrm{m\,s^{-1}}$ (Fig. 9). Forecast hour 54 was chosen as reference because it is approximately 6 h before the eye crosses the ocean boundary and is just prior to the time when the approaching cooler or warmer ocean begins to affect air–sea fluxes beneath the inner-core region of storms. At that time, the ocean boundary in these experiments is nearly 3 RMW (9 RMW) west of storm center for the large (small) storms. It is assumed that all storm adjustment occurring after hour 54 is forced by the change in SST cooling rate occurring to the west of the ocean boundary as this boundary reaches and then passes beneath the inner core.

For the large storm transitioning from cool to hot oceanic conditions (experiment DL06CH), the $\overline{v_{10}}$ increase after hour 54 is $9–10\,\mathrm{m\,s^{-1}}$ (Fig. 9a). The increase for the small storm experiment DS06CH is substantially smaller ($5–6\,\mathrm{m\,s^{-1}}$; Fig. 9d). In both cases, the largest increases are concentrated in the eyewall and the response is gradual, taking 18 h for the large storm and 12 h for the small storm after the time the eye crosses the

ocean boundary ($t = 60$) before adjustment is substantially complete. The latent component of enthalpy flux $\overline{Q_L}$ increases by $400–500\,\mathrm{W\,m^{-2}}$ in the eyewall region after hour 54 for both large and small storms. The onset of this adjustment is very rapid, beginning when the leading part of the eyewall reaches the oceanic boundary and stopping when the trailing edge of the eyewall is past the boundary, essentially over a 4-h interval for the large storm and a 2-h interval for the small storm. At larger radii from the storm center, full adjustment is delayed for a few additional hours as the ocean boundary passes under the trailing portion of the storm. Results are similar for the sensible component $\overline{Q_s}$ except that the maximum increase in the eyewall after hour 54 is smaller for both large ($100–125\,\mathrm{W\,m^{-2}}$; Figs. 9c,f) and small ($180–220\,\mathrm{W\,m^{-2}}$; Figs. 9i,l) storms.

For the large storm transitioning from hot to cool oceanic regions (experiment DL06HC), the magnitude of the $\overline{v_{10}}$ decrease after hour 54 is $12–15\,\mathrm{m\,s^{-1}}$ (Fig. 9g), a magnitude over 50% larger than the magnitude of the increase for the large storm transitioning in the opposite sense (Fig. 9a). For the small storm (experiment DS06HC), the wind speed decrease is also $12–15\,\mathrm{m\,s^{-1}}$ (Fig. 9j), more than double the magnitude of the increase for the small storm transitioning in the opposite sense. For both large and small storms, this transition occurs over a 12–18-h interval following forecast hour 60. Storms transitioning from hot to cool ocean conditions are more sensitive to the ocean than storms transitioning from cool to hot conditions.

The changes in enthalpy flux are a dominant factor in this asymmetric intensity response. The latent component $\overline{Q_L}$ decreases by $800–900\,\mathrm{W\,m^{-2}}$ in the eyewall region after hour 54 for both the large (DL06HC) and small (DS06HC) storms (Figs. 9h,k) moving from cool to hot ocean conditions. This is about double the magnitude of the increase in $\overline{Q_L}$ for both large and small storms transitioning in the opposite sense (Figs. 9b,e). This flux adjustment is again rapid compared to wind speed adjustment, but less so for storms moving from cool to hot ocean conditions compared to the opposite transition (6 vs 4 h for large storms and 10 vs 2 h for small storms). In all four cases, rapid adjustment of $\overline{Q_L}$ within the eyewall begins when the leading part of the eyewall reaches the oceanic boundary just before hour 60. For experiments DL06CH and DS06CH, adjustment within the eyewall is essentially complete when the trailing edge passes the ocean boundary. For experiments DL06HC and DS06HC, the transition takes an additional 2 and 8 h, respectively, to complete. Similar results are obtained for the sensible component $\overline{Q_s}$ except that the magnitudes are much smaller (Figs. 9c,f,i,l). The asymmetric intensity response to changing TCHP is clearly related to the
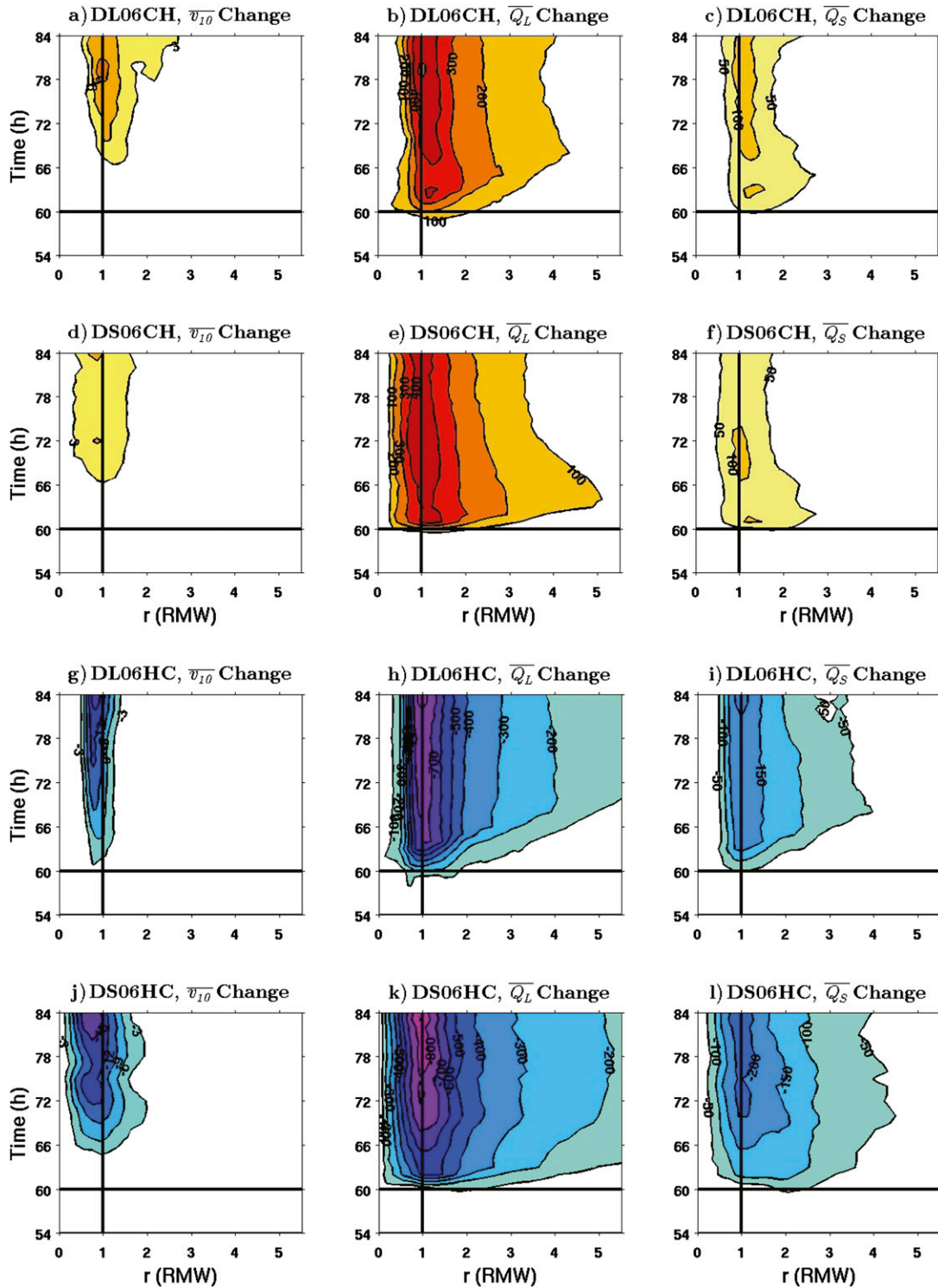
FIG. 9. Hovmöller diagrams of (left) $\overline{v_{10}}(r, t) - \overline{v_{10}}(r, 54)$, (middle) $\overline{Q_L}(r, t) - \overline{Q_L}(r, 54)$, and (right) $\overline{Q_S}(r, t) - \overline{Q_S}(r, 54)$ in W m^{-2} for several dual ocean experiments where storms transitioned from (a)–(f) cool to hot and (g)–(l) warm to cool ocean conditions at 6 m s^{-1}. Results are presented for (a)–(c) and (g)–(i) large and (d)–(f) and (j)–(l) small storms. Note the smaller contour interval for sensible flux (50 W m^{-2}) compared to latent flux (100 W m^{-2}).

asymmetric change in enthalpy flux, both the latent and sensible components.

b. Attribution of asymmetric enthalpy flux adjustments

To identify factors responsible for the asymmetry in enthalpy flux adjustments to changing TCHP, in particular emphasizing the relative roles of the atmosphere and ocean, changes in $\overline{Q_E}$ are decomposed into the part accounted for by wind speed change and the part accounted for by changes in $\overline{\Delta q}$ and $\overline{\Delta T}$ as follows: The temporal change in an azimuthally averaged arbitrary function $\overline{f}(r, t)$ over the time interval $\delta t_n = t_{n+1} - t_n$ can be written as $\delta \overline{f}(r, \delta t_n) = \overline{f}(r, t_{n+1}) - \overline{f}(r, t_n)$. If the function f is the product of two functions g and h [Eq. (6)],

and assuming that g' and h' are uncorrelated around the azimuthal axis, the temporal change in f is written as

$$\delta \overline{f}(r, \delta t_n) = \overline{g}(r, t_n) \delta \overline{h}(r, \delta t_n) + \overline{h}(r, t_n) \delta \overline{g}(r, \delta t_n) \\ + \delta \overline{g}(r, \delta t_n) \delta \overline{h}(r, \delta t_n). \tag{8}$$

If it is further assumed that g and h are linear functions of time between t_n and t_{n+1}, then

$$\delta \overline{g}(r, \delta t_n) = a(r) \delta t_n, \\ \delta \overline{h}(r, \delta t_n) = b(r) \delta t_n. \tag{9}$$

The change in the product $\overline{g}(r, t) \overline{h}(r, t)$ can then be written as

$$\delta[\overline{g}(r, \delta t_n) \overline{h}(r, \delta t_n)] = [\overline{g}(r, t_n) + a(r) \delta t_n][\overline{h}(r, t_n) + b(r) \delta t_n] - \overline{g}(r, t_n) \overline{h}(r, t_n) \\ = \overline{g}(r, t_n) b(r) \delta t_n + \overline{h}(r, t_n) a(r) \delta t_n + \delta[a(r) \delta t_n] \delta[b(r) \delta t_n] \\ = \overline{g}(r, t_n) \delta \overline{h}(r, \delta t_n) + \overline{h}(r, t_n) \delta \overline{g}(r, \delta t_n) + \delta \overline{g}(r, \delta t_n) \delta \overline{h}(r, \delta t_n). \tag{10}$$

Defining

$$\langle \overline{f} \rangle (r, t_n + \delta t_n) = \frac{1}{2}[\overline{f}(r, t_n) + \overline{f}(r, t_{n+1})] \tag{11}$$

as the temporal average of a model field between times t_n and t_{n+1}, Eq. (10) can be written as

$$\delta \overline{f}(r, \delta t_n) = \langle \overline{g} \rangle (r, t_n + \delta t_n) \delta \overline{h}(r, \delta t_n) \\ + \langle \overline{h} \rangle (r, t_n + \delta t_n) \delta \overline{g}(r, \delta t_n). \tag{12}$$

Applying Eq. (12) to Eq. (7) for $\overline{Q_E}(r, t)$ yields

$$\delta \overline{Q_E}(r) = \rho_a L_v C_k \langle \overline{v_{10}} \rangle (r, t_n + \delta t_n) \delta \overline{\Delta q}(r, \delta t_n) + \rho_a C_k \langle \overline{v_{10}} \rangle (r, t_n + \delta t_n) \delta \overline{\Delta T}(r, \delta t_n) \\ + \rho_a L_v C_k \langle \overline{\Delta q} \rangle (r, t_n + \delta t_n) \delta \overline{v_{10}}(r, \delta t_n) + \rho_a C_k \langle \overline{\Delta T} \rangle (r, t_n + \delta t_n) \delta \overline{v_{10}}(r, \delta t_n). \tag{13}$$

Changes in the latent and sensible components of the enthalpy flux over time δt_n are each represented by two terms that substantially separate the impact of changes in wind speed from changes in air–sea temperature and humidity differences. The first pair of terms on the right side of Eq. (13) represents the contribution of the change in temperature and humidity difference multiplied by the average wind speed over the specified time interval, referred to as the "air–sea part." The second pair of terms represents the contribution of the change in wind speed multiplied by the average temperature and humidity difference over the specified time interval, and is referred to as the "wind part." Both the atmosphere and ocean contribute to the changes in air–sea temperature and humidity differences used to calculate the air–sea part, and these contributions will be separated by analyzing $\delta \overline{q_s}$ and $\delta \overline{T_s}$ (the oceanic contribution) along with $\delta \overline{q_{10}}$ and $\delta \overline{T_{10}}$ (the atmospheric contribution). The accuracy of the decomposition given

by Eq. (13) depends on satisfaction of the assumptions presented in Eq. (9). Consequently, the time interval δt_n over which Eq. (13) is estimated cannot be too large.

c. Analysis of enthalpy flux adjustments after forecast hour 54

To analyze the contributions of the air–sea and wind parts of Eq. (13) to changes in $\overline{Q_E}$, forecast hour 54 is again chosen as the initial reference time. Contributions to $\overline{Q_E}(r, t) - \overline{Q_E}(r, 54)$ are then analyzed by accumulating terms on the right side of Eq. (13) over time intervals $\delta t_n = 1$ h beginning at hour 54. The total enthalpy flux change along with the separate contributions of the air–sea and wind parts are visualized in Hovmöller diagrams (Fig. 10) for the same four experiments analyzed in Fig. 9. In all cases, the change in $\overline{Q_E}$ approximately equals the sum of the air–sea and wind parts, demonstrating that hourly accumulation of terms did not violate the assumptions presented in Eq. (9).
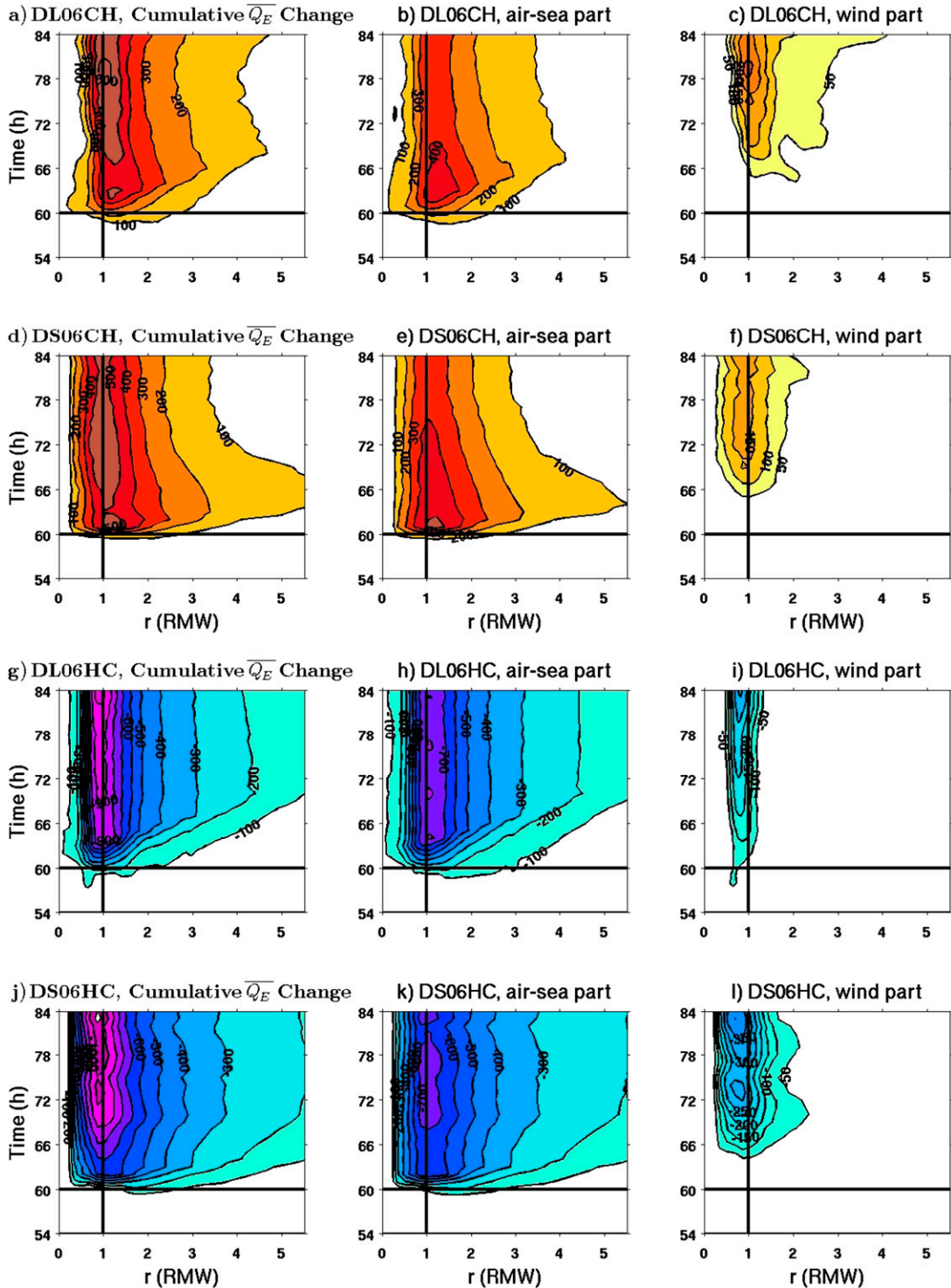
FIG. 10. Hovmöller diagrams of (left) $\overline{Q_E}(r, t) - \overline{Q_E}(r, 54)$ in W m^{-2} and its two primary components from Eq. (13): (middle) the air–sea part due to changes in Δq and ΔT and (right) the wind part due to changes in wind speed for several dual ocean experiments where storms transitioned from (a)–(f) cool to hot and (g)–(l) warm to cool ocean conditions at 6 m s^{-1}. Results are presented for (a)–(c) and (g)–(i) large and (d)–(f) and (j)–(l) small storms. Note the smaller contour interval for sensible flux (50 W m^{-2}) compared to latent flux (100 W m^{-2}).

In all four ocean transition cases, the air–sea part provides the dominant contribution to total enthalpy flux change (Fig. 10). Nearly all of the adjustment within the eyewall occurs while the eyewall is crossing the ocean boundary, over about 4 h for the large storm and 2 h for the small storm. Over an additional several hour lag, the contribution of the wind part gradually ramps up to make a significant contribution (typically 25%–30%) to the total enthalpy flux change. The initial rapid increase in the air–sea part for the two storms transitioning from cool to hot ocean conditions reverses to become a slow decrease. However, the more delayed ramp up of the wind part compensates for this reversal so that the total enthalpy flux change in the inner core remains relatively constant. For the storms transitioning from hot to cool conditions, the change in the air–sea part remains relatively constant after the initial rapid decrease. As the contribution of the wind part increases over the next several hours, the total enthalpy flux decrease in the eyewall continues to become larger with time. Concerning the asymmetric response magnitude, both the air–sea and wind parts contribute to the larger enthalpy flux decrease for storms transitioning from hot to cool ocean conditions. The maximum change of the air–sea part equals 450 W m^{-2} for experiment DL06CH and -800 W m^{-2} for experiment DL06HC, and equals 500 W m^{-2} for experiment DS06CH and -750 W m^{-2} for experiment DS06HC. The initial forcing of this asymmetric response is provided by the air–sea part, but the wind part also contributes significantly as it ramps up due to the larger intensity changes in experiments DL06HC and DS06HC compared to DL06CH and DS06CH.

Analyses are performed on these four transition cases to separate the atmospheric and oceanic contributions to the asymmetric response of the air–sea part of $\overline{Q_E}$ by constructing Hovmöller diagrams of changes in $\overline{\Delta q}$, $\overline{q_s}$, and $\overline{q_{10}}$ (Fig. 11), and in $\overline{\Delta T}$, $\overline{T_s}$, and $\overline{T_{10}}$ (Fig. 12). Decreases in $\overline{\Delta q}$ and $\overline{\Delta T}$ after forecast hour 54 for storms transitioning from hot to cool ocean conditions are both much larger than the increases for storms transitioning in the opposite sense. Both ocean and atmosphere contribute to this asymmetry. For the ocean, the decrease in $\overline{q_s}$ is modestly larger (~25%) for the small storm, and substantially larger (~60%) for the large storm, transitioning from hot to cool conditions compared to the corresponding increases for storms transitioning in the opposite sense (Fig. 11). Also, the decrease in $\overline{T_s}$ is slightly larger (~10%) for the small storm, and only modestly larger (~20%) for the large storm transitioning from hot to cool conditions compared to the corresponding increases for storms transitioning in the opposite sense (Fig. 12).

The greater asymmetry in the $\overline{q_s}$ change compared to the $\overline{T_s}$ change results from the large sensitivity of evaporation rate to small changes in $\overline{T_s}$ at high temperature values.

The atmospheric feedback response through changes in $\overline{q_{10}}$ and $\overline{T_{10}}$ after forecast hour 54 always acts to reduce the magnitudes of the $\overline{\Delta q}$ and $\overline{\Delta T}$ responses. This result is consistent with the atmospheric influence on limiting differences in quasi-equilibrium intensity in the uniform ocean experiments (Figs. 6 and 7). This passive feedback response demonstrates that the idealized representation of the atmosphere successfully suppressed the impact of large-scale atmospheric processes that force intensity change in the real world. Active atmospheric forcing as documented in the observational analyses of Cione et al. (2013) and Cione (2015) is not detectable in the present study. At radii within and outside of the eyewall, the increases in $\overline{q_{10}}$ and $\overline{T_{10}}$ after forecast hour 54 are much larger in magnitude for storms transitioning from cool to hot ocean conditions compared to the decreases for storms transitioning in the opposite sense. This atmospheric response substantially reduces the increases in $\overline{\Delta q}$ and $\overline{\Delta T}$ for storms transitioning from cool to hot conditions, thus reversing the initial rapid increase in $\overline{Q_E}$.

Except for $\overline{q_{10}}$ in the transition from hot to cool conditions, the time scales of the $\overline{q_{10}}$ and $\overline{T_{10}}$ responses are substantially longer compared to the corresponding surface ocean fields. The ocean response occurs primarily in the cold wake and is comparatively rapid. By contrast, the time scale of the azimuthally averaged atmospheric response must take into account the time scale required for atmospheric adjustments forced over the cold wake to advect around the storm. Overall, these results demonstrate that the air–sea interactions that control intensity are fundamentally a coupled problem, even in the highly idealized setting of this study.

The atmospheric and oceanic contributions to the asymmetric intensity response to increasing and decreasing TCHP are summarized as follows: First, when a storm in quasi-equilibrium with a hot ocean initially encounters lower TCHP, larger wind speed is present causing the increased SST cooling rate to produce a larger reduction in enthalpy flux compared to the opposite situation. These flux adjustments occur rapidly and produce intensity adjustments over a time interval up to 18 h. These intensity adjustments further increase the asymmetric response of enthalpy flux because wind speed decreases more for storms encountering smaller TCHP than it increases for storms encountering higher TCHP. The atmospheric feedback through $\overline{q_{10}}$ and $\overline{T_{10}}$ is a third factor that contributes to the asymmetry in the magnitude of enthalpy flux adjustment. The $\overline{q_{10}}$ changes
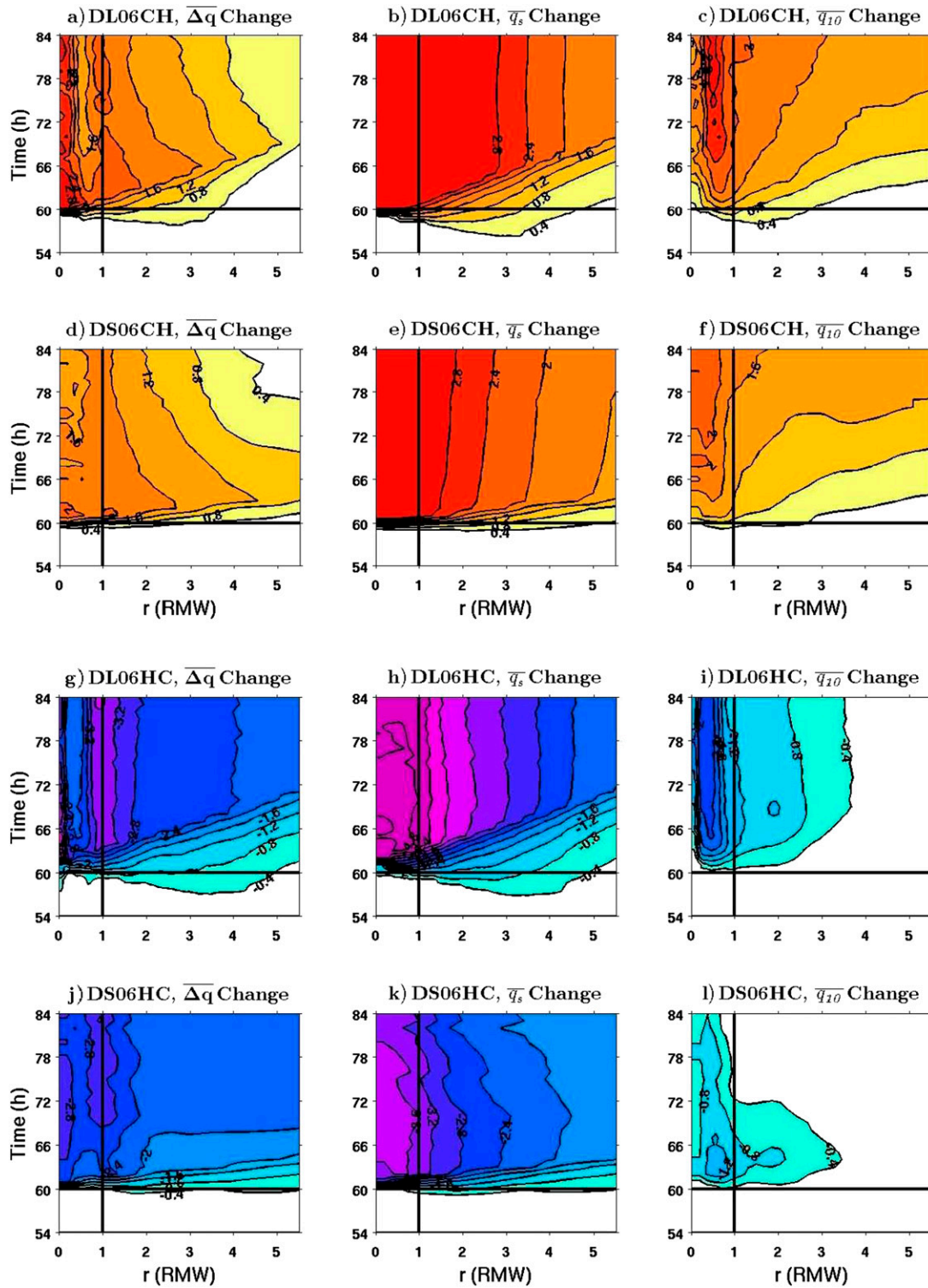
FIG. 11. Hovmöller diagrams of (left) $\overline{\Delta q}(r, t) - \overline{\Delta q}(r, 54)$, (middle) $\overline{q_s}(r, t) - \overline{q_s}(r, 54)$, and (right) $\overline{q_{10}}(r, t) - \overline{q_{10}}(r, 54)$ in $g\,kg^{-1}$ for several dual ocean experiments where storms transitioned from (a)–(f) cool to hot and (g)–(l) warm to cool ocean conditions at $6\,m\,s^{-1}$. Results are presented for (a)–(c) and (g)–(i) large and (d)–(f) and (j)–(l) small storms.
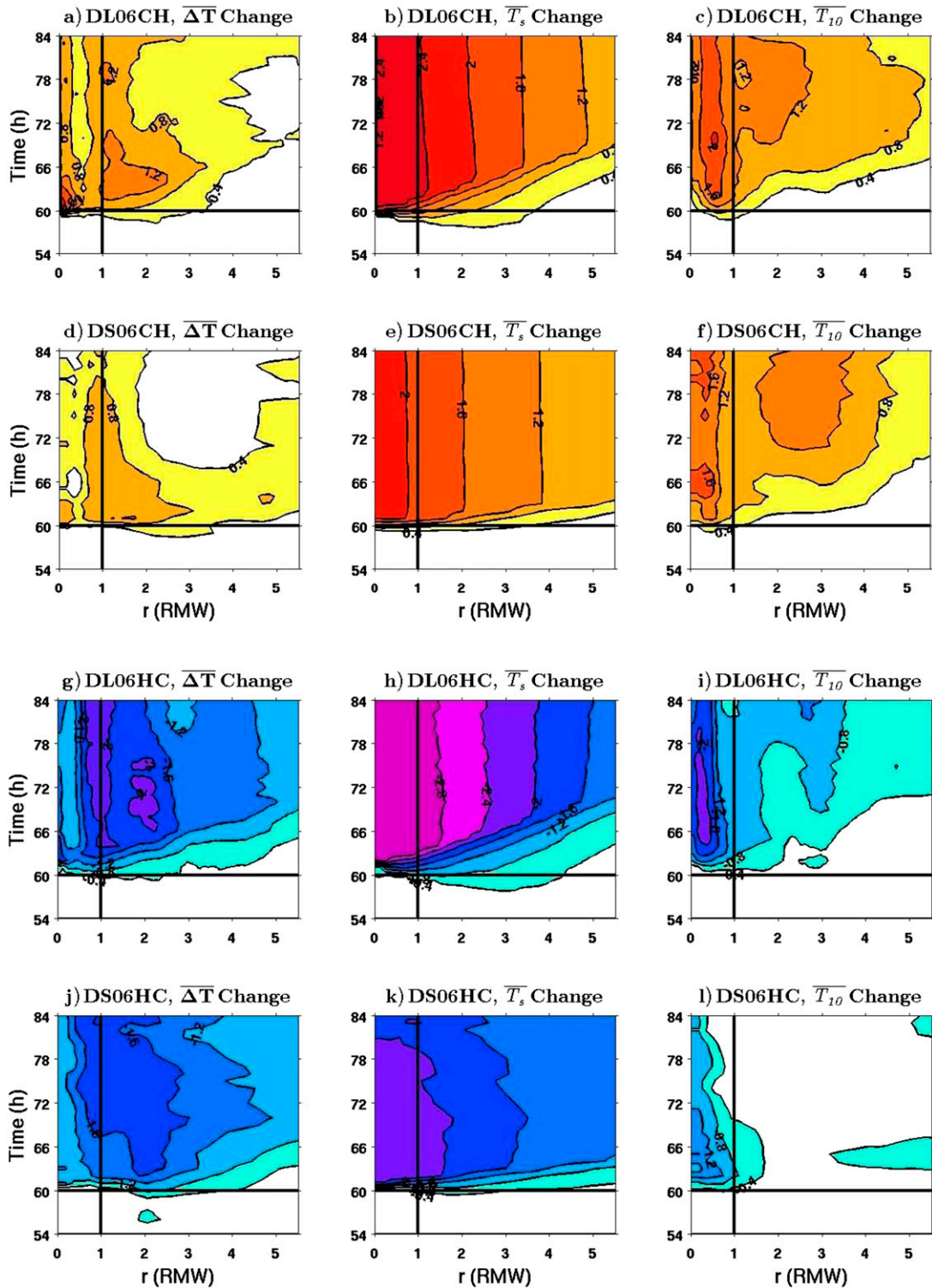
FIG. 12. As in Fig. 11, but showing Hovmöller diagrams of (left) $\overline{\Delta T}(r, t) - \overline{\Delta T}(r, 54)$, (middle) $\overline{T_s}(r, t) - \overline{T_s}(r, 54)$, and (right) $\overline{T_{10}}(r, t) - \overline{T_{10}}(r, 54)$ in °C.

for storms encountering decreasing TCHP are smaller than the changes for storms encountering increasing TCHP. This acts to further reduce the $\overline{\Delta Q_E}$ change for storms encountering larger TCHP, thus increasing the asymmetric response.

6. Summary and conclusions

The present idealized study was designed to obtain an improved understanding of the sensitivity of the HWRF model to ocean cooling. A one-dimensional ocean model is embedded in version 3.2 of the HWRF atmospheric model, which is run over a 27-km parent domain with two (9 and 3 km) movable nests, essentially the same atmospheric model used operationally prior to the 2013 TC season. Coupled TC simulations are conducted in a setting designed to isolate the impact of ocean cooling while the impact of large-scale atmospheric processes on intensity change, such as dry air entrainment and wind shear, is effectively eliminated. The idealized atmosphere is horizontally uniform and is initialized by superimposing an idealized vortex that can draw upon an essentially infinite supply of deep tropical moisture in the far field. The initial ocean is horizontally uniform with no land, and westward storm translation is accounted for by bodily advecting ocean fields to the east at discrete times. Experiments to study the impact of the ocean on quasi-equilibrium intensity are initialized with an ocean that is horizontally uniform throughout the parent domain. Experiments to study the impact of changing ocean conditions are initialized with an ocean containing two horizontally uniform regions separated by a meridional boundary that passes beneath the storm during simulations.

Although the one-dimensional ocean model does not reproduce important three-dimensional processes such as upwelling, it does produce a cold wake on the innermost nest that is sufficiently realistic to characterize HWRF sensitivity to ocean cooling and identify key processes controlling this sensitivity. Because this is a highly idealized study, the emphasis is on documenting model sensitivity to a broad range of SST cooling rates as opposed to accurately reproducing phenomena that occur in nature. Parameter dependence of quasi-equilibrium storm intensity produced by HWRF generally followed expected behavior. Small and faster-moving simulated storms are less sensitive to the ocean, as are storms passing over oceanic regions with thick warm layers and high TCHP. Both small and large storms are more sensitive to TCHP than to translation speed. For storms translating at $>2\,\mathrm{m\,s^{-1}}$, ocean impact on quasi-equilibrium intensity is minimal for storms traveling over regions with TCHP $> 85\,\mathrm{kJ\,cm^{-2}}$, more so for small storms compared to large ones. Inner-core ($r \lesssim 3$ RMW)

cooling is limited (average of $<1°C$) for medium-to-large values of prestorm TCHP, but increases to $>2°C$ when TCHP is small ($\sim 25\,\mathrm{kJ\,cm^{-2}}$).

A key goal of the present analysis is to identify atmospheric and oceanic processes that control this sensitivity. The atmospheric contribution to quasi-equilibrium intensity in this idealized setting is to provide feedback through adjustments in 10-m temperature and humidity that reduces the impact of different SST cooling rates on enthalpy flux by up to 40%. When a TC travels over an oceanic region with different TCHP, the enthalpy flux adjustment is governed primarily by changes in air–sea temperature and humidity differences. These responses occur within 2–4 h inside the inner-core region of the TC. The enthalpy flux adjustment is driven secondarily by wind speed changes that occur over a time interval of up to 18 h. The smaller time scale for flux adjustment occurs when the eyewall region with the strongest winds passes the ocean heat potential boundary while the atmospheric response forced by the cold wake requires additional time to advect around the storm circumference. When ocean conditions change, atmospheric feedback always acts to limit the resulting enthalpy flux and intensity responses through adjustments in 10-m temperature and humidity.

Intensity change is asymmetric, with increases for storms encountering larger heat potential being substantially smaller than decreases for storms encountering smaller heat potential. The smaller decrease results initially from the smaller wind speed present at the time the oceanic change is encountered, which reduces the impact of changes in air–sea temperature and humidity differences, and is then supplemented by a stronger limiting atmospheric feedback. The smaller wind speed increase resulting from these two factors further enhances the asymmetry. Even in this highly idealized study, storm intensity is fundamentally governed by coupled air–sea interaction processes. By minimizing the impact of large-scale atmospheric processes that force intensity changes, it is possible to obtain a clearer view of how atmospheric feedback tends to limit intensity changes forced by changes in SST cooling beneath the inner core of storms.

REFERENCES

Bao, J.-W., S. G. Gopalakrishnan, S. A. Michelson, F. D. Marks, and M. T. Montgomery, 2012: Impact of physics representations in

the HWRFX on simulated hurricane structure and pressure–wind relationships. *Mon. Wea. Rev.,* **140,** 3278–3299, doi:10.1175/MWR-D-11-00332.1.

Bleck, R., 2002: An oceanic general circulation framed in hybrid isopycnic-Cartesian coordinates. *Ocean Modell.,* **4,** 55–88, doi:10.1016/S1463-5003(01)00012-9.

Chang, S. W.-J., 1979: The response of an axisymmetric model tropical cyclone to local variations of sea surface temperature. *Mon. Wea. Rev.,* **107,** 662–666, doi:10.1175/1520-0493(1979)107<0662:TROAAM>2.0.CO;2.

Chassignet, E. P., H. E. Hurlburt, O. M. Smedstad, G. R. Halliwell, P. J. Hogan, A. J. Wallcraft, R. Baraille, and R. Bleck, 2007: The HYCOM (Hybrid Coordinate Ocean Model) data assimilative system. *J. Mar. Syst.,* **65,** 60–83, doi:10.1016/j.jmarsys.2005.09.016.

Chiang, T.-L., C.-R. Wu, and L.-Y. Oey, 2011: Typhoon Kai-Tak: An ocean's perfect storm. *J. Phys. Oceanogr.,* **41,** 221–233, doi:10.1175/2010JPO4518.1.

Cione, J. J., 2015: The relative roles of the ocean and atmosphere as revealed by buoy air–sea observations in hurricanes. *Mon. Wea. Rev.,* **143,** 904–913, doi:10.1175/MWR-D-13-00380.1.

——, and E. W. Uhlhorn, 2003: Sea surface temperature variability in hurricanes: Implications with respect to intensity change. *Mon. Wea. Rev.,* **131,** 1783–1796, doi:10.1175//2562.1.

——, E. A. Kalina, J. A. Zhang, and E. W. Uhlhorn, 2013: Observations of air–sea interaction and intensity change in hurricanes. *Mon. Wea. Rev.,* **141,** 2368–2382, doi:10.1175/MWR-D-12-00070.1.

DeMaria, M., M. Mainelli, L. K. Shay, J. A. Knaff, and J. Kaplan, 2005: Further improvements to the Statistical Hurricane Intensity Prediction Scheme (SHIPS). *Wea. Forecasting,* **20,** 531–543, doi:10.1175/WAF862.1.

Elsberry, R., T. Fraim, and R. Trapnell Jr., 1976: A mixed layer model of the oceanic thermal response to hurricanes. *J. Geophys. Res.,* **81,** 1153–1162, doi:10.1029/JC081i006p01153.

Emanuel, K. A., 1988: The maximum intensity of hurricanes. *J. Atmos. Sci.,* **45,** 1143–1155, doi:10.1175/1520-0469(1988)045<1143:TMIOH>2.0.CO;2.

——, C. DesAutels, C. Holloway, and R. Korty, 2004: Environmental controls of tropical cyclone intensity. *J. Atmos. Sci.,* **61,** 843–858, doi:10.1175/1520-0469(2004)061<0843:ECOTCI>2.0.CO;2.

Goni, G. J., and J. A. Trinanes, 2003: Ocean thermal structure monitoring could aid in the intensity forecast of tropical cyclones. *Eos, Trans. Amer. Geophys. Union,* **84,** 573–578, doi:10.1029/2003EO510001.

——, and Coauthors, 2009: Applications of satellite-derived ocean measurements to tropical cyclone intensity forecasting. *Oceanography,* **22,** 190–197, doi:10.5670/oceanog.2009.78.

Gopalakrishnan, S. G., X. Zhang, J.-W. Bao, K.-S. Yeh, and R. Atlas, 2011: The experimental HWRF system: A study on the influence of horizontal resolution on the structure and intensity changes in tropical cyclones using an idealized framework. *Mon. Wea. Rev.,* **139,** 1762–1784, doi:10.1175/2010MWR3535.1.

——, F. Marks Jr., J. A. Zhang, X. Zhang, J.-W. Bao, and V. Tallapragada, 2013: A study of the impacts of vertical diffusion on the structure and intensity of the tropical cyclones using the high-resolution HWRF system. *J. Atmos. Sci.,* **70,** 524–541, doi:10.1175/JAS-D-11-0340.1.

Greatbatch, R. J., 1984: On the response of the ocean to a moving storm: Parameters and scales. *J. Phys. Oceanogr.,* **14,** 59–78, doi:10.1175/1520-0485(1984)014<0059:OTROTO>2.0.CO;2.

——, 1985: On the role played by upwelling of water in lowering sea surface temperatures during the passage of a storm. *J. Geophys. Res.,* **90,** 11 751–11 755, doi:10.1029/JC090iC06p11751.

Halliwell, G. R., Jr., 2004: Evaluation of vertical coordinate and vertical mixing algorithms in the Hybrid-Coordinate Ocean Model (HYCOM). *Ocean Modell.,* **7,** 285–322, doi:10.1016/j.ocemod.2003.10.002.

Holland, G. J., 1997: The maximum potential intensity of tropical cyclones. *J. Atmos. Sci.,* **54,** 2519–2541, doi:10.1175/1520-0469(1997)054<2519:TMPIOT>2.0.CO;2.

Hong, X., S. W. Chang, S. Raman, L. K. Shay, and R. Hodur, 2000: The interaction between Hurricane Opal (1995) and a warm core ring in the Gulf of Mexico. *Mon. Wea. Rev.,* **128,** 1347–1365, doi:10.1175/1520-0493(2000)128<1347:TIBHOA>2.0.CO;2.

Ito, K., T. Kuroda, K. Saito, and A. Wada, 2015: Forecasting a large number of tropical cyclone intensities around Japan using a high-resolution atmosphere–ocean coupled model. *Wea. Forecasting,* doi:10.1175/WAF-D-14-00034.1, in press.

Jacob, S. D., and L. K. Shay, 2003: The role of oceanic mesoscale features on the tropical cyclone–induced mixed layer response. *J. Phys. Oceanogr.,* **33,** 649–676, doi:10.1175/1520-0485(2003)33<649:TROOMF>2.0.CO;2.

——, ——, A. J. Mariano, and P. G. Black, 2000: The 3-D oceanic mixed-layer response to Hurricane Gilbert. *J. Phys. Oceanogr.,* **30,** 1407–1429, doi:10.1175/1520-0485(2000)030<1407:TOMLRT>2.0.CO;2.

Jaimes, B., and L. K. Shay, 2009: Mixed layer cooling in mesoscale ocean eddies during Hurricanes Katrina and Rita. *Mon. Wea. Rev.,* **137,** 4188–4207, doi:10.1175/2009MWR2849.1.

——, and ——, 2010: Near-inertial wave wake of Hurricanes Katrina and Rita over mesoscale oceanic eddies. *J. Phys. Oceanogr.,* **40,** 1320–1337, doi:10.1175/2010JPO4309.1.

Kim, H.-S., C. Lozano, V. Tallapragada, D. Iredell, D. Sheinin, H. L. Tolman, V. M. Gerald, and J. Sims, 2014: Performance of ocean simulations in the coupled HWRF-HYCOM model. *J. Atmos. Oceanic Technol.,* **31,** 545–559, doi:10.1175/JTECH-D-13-00013.1.

Large, W. G., J. C. McWilliams, and S. C. Doney, 1994: Oceanic vertical mixing: A review and a model with a nonlocal boundary layer parameterization. *Rev. Geophys.,* **32,** 363–403, doi:10.1029/94RG01872.

Leipper, D. F., and D. Volgenau, 1972: Hurricane heat potential of the Gulf of Mexico. *J. Phys. Oceanogr.,* **2,** 218–224, doi:10.1175/1520-0485(1972)002<0218:HHPOTG>2.0.CO;2.

Lin, I.-I., C.-C. Wu, K. A. Emmanuel, I.-H. Lee, C.-R. Wu, and I.-F. Pun, 2005: The interaction of Supertyphoon Maemi (2003) with a warm ocean eddy. *Mon. Wea. Rev.,* **133,** 2635–2649, doi:10.1175/MWR3005.1.

——, ——, I.-F. Pun, and D.-S. Ko, 2008: Upper-ocean thermal structure and the western North Pacific category 5 typhoons. Part I: Ocean features and the category 5 typhoons' intensification. *Mon. Wea. Rev.,* **136,** 3288–3306, doi:10.1175/2008MWR2277.1.

——, C.-H. Chen, I.-F. Pun, W. T. Liu, and C.-C. Wu, 2009a: Warm ocean anomaly, air–sea fluxes, and the rapid intensification of Tropical Cyclone Nargis (2008). *Geophys. Res. Lett.,* **36,** L03817, doi:10.1029/2008GL035815.

——, I.-F. Pun, and C.-C. Wu, 2009b: Upper-ocean thermal structure and the western North Pacific category 5 typhoons. Part II: Dependence on translation speed. *Mon. Wea. Rev.,* **137,** 3744–3757, doi:10.1175/2009MWR2713.1.

——, G. A. Goni, J. A. Knaff, C. Forbes, and M. M. Ali, 2013: Ocean heat content for tropical cyclone intensity forecasting and its impact on storm surge. *Nat. Hazards,* **66,** 1481–1500, doi:10.1007/s11069-012-0214-5.

Lloyd, I. D., and G. A. Vecchi, 2011: Observational evidence for oceanic controls on hurricane intensity. *J. Climate,* **24,** 1138–1153, doi:10.1175/2010JCLI3763.1.

Mainelli, M., M. DeMaria, L. K. Shay, and G. Goni, 2008: Application of oceanic heat content estimation to operational forecasting of recent category 5 hurricanes. *Wea. Forecasting,* **23,** 3–16, doi:10.1175/2007WAF2006111.1.

Mei, W., C. Pasquero, and F. Primeau, 2012: The effect of translation speed upon the intensity of tropical cyclones over the tropical ocean. *Geophys. Res. Lett.,* **39,** L07801, doi:10.1029/2011GL050765.

Miller, B. I., 1958: On the maximum intensity of hurricanes. *J. Meteor.,* **15,** 184–195, doi:10.1175/1520-0469(1958)015<0184: OTMIOH>2.0.CO;2.

Price, J. F., 1981: Upper ocean response to a hurricane. *J. Phys. Oceanogr.,* **11,** 153–175, doi:10.1175/1520-0485(1981)011<0153: UORTAH>2.0.CO;2.

——, 2009: Metrics of hurricane–ocean interaction: Vertically-integrated or vertically-averaged ocean temperature? *Ocean Sci.,* **5,** 351–368, doi:10.5194/os-5-351-2009.

Schade, L. R., and K. A. Emanuel, 1999: The ocean's effect on the intensity of tropical cyclones: Results from a simple coupled atmosphere–ocean model. *J. Atmos. Sci.,* **56,** 642–651, doi:10.1175/1520-0469(1999)056<0642:TOSEOT>2.0.CO;2.

Scharroo, R., W. H. Smith, and J. L. Lillibridge, 2005: Satellite altimetry and the intensification of Hurricane Katrina. *Eos, Trans. Amer. Geophys. Union,* **86,** 366–367, doi:10.1029/2005EO400004.

Shay, L. K., 2009: Upper ocean structure: Response to strong forcing events. *Encyclopedia of Ocean Sciences,* 2nd ed. J. Steele et al., Eds., Elsevier, 192–210, doi:10.1016/B978-012374473-9.00628-7.

——, and J. K. Brewster, 2010: Oceanic heat content variability in the eastern Pacific Ocean for hurricane intensity forecasting. *Mon. Wea. Rev.,* **138,** 2110–2131, doi:10.1175/2010MWR3189.1.

——, P. G. Black, A. J. Mariano, J. D. Hawkins, and R. L. Elsberry, 1992: Upper ocean response to Hurricane Gilbert. *J. Geophys. Res.,* **97,** 20 277–20 248, doi:10.1029/92JC01586.

——, G. J. Goni, and P. G. Black, 2000: Effects of a warm oceanic feature on Hurricane Opal. *Mon. Wea. Rev.,* **128,** 1366–1383, doi:10.1175/1520-0493(2000)128<1366:EOAWOF>2.0.CO;2.

Sun, D., R. Gautam, G. Cervone, Z. Boyeyi, and M. Kaptos, 2006: Comment on "Satellite altimetry and the intensification of Hurricane Katrina." *Eos, Trans. Amer. Geophys. Union,* **87,** 89, doi:10.1029/2006EO080006.

Suzuki, S., H. Niino, and R. Kimura, 2011: The mechanism of upper-oceanic vertical motions forced by a moving typhoon. *Fluid Dyn. Res.,* **43,** 025504, doi:10.1088/0169-5983/43/2/025504.

Vincent, E. M., M. Lengaigne, J. Vialard, G. Madec, N. C. Jourdain, and S. Masson, 2012: Assessing the oceanic control on the amplitude of sea surface cooling induced by tropical cyclones. *J. Geophys. Res.,* **117,** C05023, doi:10.1029/2011JC007705.

Wada, A., and N. Usui, 2007: Importance of tropical cyclone heat potential for tropical cyclone intensity and intensification in the western North Pacific. *J. Oceanogr.,* **63,** 427–447, doi:10.1007/s10872-007-0039-0.

Walker, N., R. R. Leben, and S. Balasubramanian, 2005: Hurricane forced upwelling and chlorophyll *a* enhancement within cold core cyclones in the Gulf of Mexico. *Geophys. Res. Lett.,* **32,** L18610, doi:10.1029/2005GL023716.

Wu, C.-C., C.-Y. Lee, and I.-I. Lin, 2007: The effect of the ocean eddy on tropical cyclone intensity. *J. Atmos. Sci.,* **64,** 3562–3578, doi:10.1175/JAS4051.1.

Wu, C.-R., Y.-L. Chang, L.-Y. Oey, C.-W. J. Chang, and Y.-C. Hsin, 2008: Air–sea interaction between Tropical Cyclone Nari and Kuroshio. *Geophys. Res. Lett.,* **35,** L12605, doi:10.1029/2008GL033942.

Xu, J., and Y. Wang, 2010: Sensitivity of tropical cyclone inner-core size and intensity to the radial distribution of surface entropy flux. *J. Atmos. Sci.,* **67,** 1831–1852, doi:10.1175/2010JAS3387.1.

Yablonsky, R. M., and I. Ginis, 2009: Limitation of one-dimensional ocean models for coupled ocean–hurricane model forecasts. *Mon. Wea. Rev.,* **137,** 4410–4419, doi:10.1175/2009MWR2863.1.

Zhang, X., T. Quirino, K.-S. Yeh, S. Gopalakrishnan, F. Marks, S. Goldenberg, and S. Aberson, 2011: HWRFx: Improving hurricane forecasts with high-resolution modeling. *Comput. Sci. Eng.,* **13,** 13–21, doi:10.1109/MCSE.2010.121.